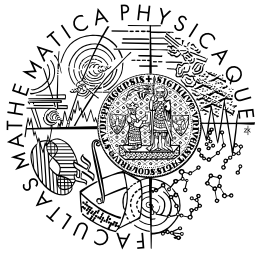

FACULTY
OF MATHEMATICS
AND PHYSICS
Charles University

MASTER THESIS

David Sviták

Study of spin-waves in the triangular lattice antiferromagnetic systems

Department of Condensed Matter Physics

Supervisor of the master thesis: RNDr. Michal Vališka, Ph.D.

Study programme: Physics of Condensed Matter and Materials

Study branch: FKSMP

Prague 2024

I declare that I carried out this master thesis independently, and only with the cited sources, literature and other professional sources. It has not been used to obtain another or the same degree.

I understand that my work relates to the rights and obligations under the Act No. 121/2000 Sb., the Copyright Act, as amended, in particular the fact that the Charles University has the right to conclude a license agreement on the use of this work as a school work pursuant to Section 60 subsection 1 of the Copyright Act.

In ..... date ....

Author's signature

First of all I would like to thank my supervisor RNDr. Michal Vališka, Ph.D. for advice, time and overall help with my masters thesis. I would also like to thank RNDr. Petr Čermák, Ph.D. who was consultant of my thesis and provided valuable insight into neutron data refinement and was lead developer of ALSA.
I would like to thank the development team of ALSA namely bc. Štěpán Venclík and bc. Tomáš Červeň who created the camera vision system for ALSA and movement protocol of robotic arm in ALSA.
I would like to also thank Nikolaos Biniskos, Ph.D. who performed the neutron experiment at ILL and Dr. Karin Schmalzl who was the instrument responsible for IN12.
I would like to thank my family for the relentless support.

Title: Study of spin-waves in the triangular lattice antiferromagnetic systems

Author: David Sviták

Department: Department of Condensed Matter Physics

Supervisor: RNDr. Michal Vališka, Ph.D., Department of Condensed Matter Physics

Abstract: The content of this work is a measurement of spin waves in triangular lattice antiferromagnets. Single crystals of $Na_2BaMn(PO_4)_2$ were successfully grown and the magnetic properties of this system were initially studied by the specific heat with applied magnetic field along *ab* and *c* axis. These measurements revealed a rich magnetic phase diagram with a new phase, that might be a highly exotic Vortex crystal phase. Complementary inelastic neutron scattering studies of this system could be performed only thanks to the development and improvement of the new experimental technique called Automatic Laue Sample Aligner (ALSA). After several tests and improvements, we used this device to automatically coalign hundreds of milligram crystals to form a large enough sample. Such an advanced approach led to the impressive mosaicity spread around 2° and thus to a very sensitive inelastic neutron study performed on IN12 at Institute Laue-Langevin. It allowed us to determine the propagation vector in the ground state at 55 mK as $k = (1/3, 1/3, \pm 0.181(4))$. Additionally, spin waves were measured in a fully polarized state in a magnetic field of 10 T revealing magnon dispersion in $Na_2BaMn(PO_4)_2$.

Keywords: Spin waves, Frustrated systems, Triangular lattice, Antiferromagnetism

Contents

Introduction

Two-dimensional triangular lattice antiferromagnetic systems are perfect representation of geometrical frustrated magnetism (1). The magnetic phase diagram of a two-dimensional triangular lattice antiferromagnetic system has been earlier studied theoretically revealing the coplanar phase 120° phase in ground state that evolves into Y, up-up-down (UUD), and V phase upon increasing magnetic field and temperature (2).

There are not many two-dimensional antiferromagnetic systems that exhibit magnetic phase diagram proposed. In practice, not as many two-dimensional triangular lattice Heisenberg antiferromagnetic systems follow the proposed model and different perturbations can destroy or modify the ideal ground state, such as anisotropy (3), next-nearest-neighbor (4) or inter-layer interactions (5). Compounds $Na_2BaX(PO_4)_2$ (X = Co, Ni, Mn) were reported to show frustrated magnetism on the triangular lattice with spins 1/2, 1, and 5/2 respectively. All three compounds host the UUD phase (6; 7; 8) and their phase diagrams show promising conditions for hosting the quantum spin liquid phase. To prove or disprove the quantum spin liquid phase one must measure the magnetic excitations of ground state using inelastic neutron scattering, which proves to be experimentally very complicated.

Single crystals of compounds $Na_2BaX(PO_4)_2$ (X = Co, Ni, Mn) are generally very small with an average mass of 10 mg, which is not enough for inelastic neutron experiment. Traditionally, experimental physicists are coaligning big amount of single crystals in order to have higher inelastic signal (9). This process is very time-consuming, demanding, and could suffer from low precision[1]. For this reason, we developed a new experimental technique for crystal coalignment called Automatic Laue Sample Aligner (ALSA). ALSA combines a robotic arm, camera vision, and Laue diffractometer to coalign crystals automatically. The whole coalignment process is one of the key parts of this thesis.

ALSA provides not only acceleration of the production process of samples for inelastic neutron experiments but also improvement in the quality and precision of the production process. Using ALSA it would be possible to distinguish complicated spin wave dispersions that were previously hidden in the elastic signal. In this thesis, we present inelastic neutron measurement on multiple samples prepared by ALSA demonstrating its capabilities.

[1]Private communications with Huiqian Luo, one of the authors of (9)

1 Theory

1.1 Magnetism

The magnetic moment in magnetism is the fundamental object, which can be defined as (10)

$$\overrightarrow{d\mu} = I\overrightarrow{dS} \tag{1.1}$$

where I is current going trough the oriented loop of area $\overrightarrow{dS}$ and magnetic moment μ has units of Am^2. In solid-state physics, it is much more convenient to use Bohr magneton since it describes the magnetic moment at the atomic level. It is described as

$$\mu_B = \frac{e\hbar}{2m_e} \tag{1.2}$$

A magnetic solid consists of a large number of these current loops with magnetic moments. The magnetization $\overrightarrow{M}$ is defined as the magnetic moment per unit volume and defines the vector field inside the solid. In special case magnetization $\overrightarrow{M}$ is linearly related to the magnetic field $\overrightarrow{H}$, the solid is called linear material, and we can write

$$\overrightarrow{M} = \chi\overrightarrow{H} \tag{1.3}$$

where χ is the dimensionless quantity called the magnetic susceptibility.
The electronic angular momentum defined by equation 1.1 is associated with the orbital motion of an electron around the nucleus. In a real atom, it depends on the electronic state occupied by the electron. In addition electron possesses an intrinsic magnetic moment which is associated with intrinsic angular momentum. This intrinsic angular momentum of an electron is called spin. The magnetic moment on an atom is associated with its total angular momentum $\overrightarrow{J}$ which is determined by the third Hunds rule (11). We can calculate total angular momentum from orbital angular momentum $\overrightarrow{L}$ and the spin angular momentum $\overrightarrow{S}$.

1.2 Order and magnetic structure

In the previous section, we introduced the magnetism of free ions. However, for magnetic ions in certain materials one cannot usually ignore interactions between magnetic ions. In this section, we will introduce different types of interactions that can lead to long range order, which we also parameterise.

1.2.1 Interactions

One of the most fundamental interactions between two magnetic dipoles $\overrightarrow{\mu}_1$ and $\overrightarrow{\mu}_2$ is the **magnetic dipolar interaction**, which have energy equal to

$$E = \frac{\mu_0}{4\pi r^3}\left[\overrightarrow{\mu}_1 \cdot \overrightarrow{\mu}_2 - \frac{3}{r^2}\left(\overrightarrow{\mu}_1 \cdot \overrightarrow{r}\right)\left(\overrightarrow{\mu}_2 \cdot \overrightarrow{r}\right)\right] \tag{1.4}$$

which depends on their separation and their degree of mutual alignment. This interaction is weak compared to others and interaction energy is equivalent to

about 1 K in temperature.
Exchange interactions are mostly responsible for phenomena associated with long range magnetic order. Exchange interactions are electrostatic interactions and can be described by Heisenberg Hamiltonian (12)

$$\hat{H} = -2\sum_{i<j} J_{ij} \overrightarrow{S}_i \cdot \overrightarrow{S}_j \tag{1.5}$$

where J_{ij} is exchange constant between the i^{th} and j^{th} spin and $i < j$ prevents the double-counting. Often it is possible to take J_{ij} to be equal to a constant for nearest neighbour spins and to be 0 otherwise, which is called nearest neighbor approximation.
If the electrons on neighboring magnetic atoms interact via an exchange interaction (see figure 1.1), this is known as **direct exchange**. Thus we can classify this interaction as a short range. This is the case when the wave functions of neighboring magnetic atoms have sufficient overlap and the exchange integral reaches values around 10^2-10^3 K.

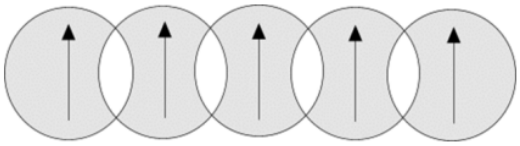

Figure 1.1: Schematic picture of the direct exchange interaction. Arrows represent magnetic moments. (13)

Indirect exchange interaction (also called superexchange) is a mechanism that takes place between the non-neighboring magnetic ions and is mediated by non-magnetic ions between them. Indirect exchange can be found in ionic compounds such as oxides and fluorides and is usually mediated by p and d - elements such as oxygen. This exchange is Schematic of this mechanism is shown in figure 1.2. The magnitude of this interaction is usually lower than in the case of direct exchange, typically around 10^0-10^2 K.
There is another indirect exchange called Ruderman–Kittel–Kasuya–Yosida (RKKY)

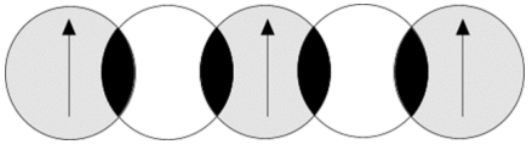

Figure 1.2: Schematic picture of the indirect exchange interaction. Arrows represent magnetic moments. (13)

interaction. This interaction is mediated by the conduction electrons, which make it relevant interaction in metals.

1.2.2 Magnetic structures

Let us consider the different types of magnetic ground states that can be produced by interactions described in section 1.2.1.

A **ferromagnet** is a ground state in which adjacent magnetic moments are in parallel alignment as illustrated in figure 1.3a, which results in spontaneous magnetization in the absence of an applied field. Ferromagnetism is generally caused by exchange interaction and the appropriate Hamiltonian (10) to sole in applied magnetic field $\overrightarrow{B}$ is

$$\hat{H} = -\sum_{ij} J_{ij} \overrightarrow{S}_i \cdot \overrightarrow{S}_j + g\mu_B \sum_j \overrightarrow{S}_j \overrightarrow{B} \tag{1.6}$$

and the exchange constant, defined in equation 1.5, for neighbors will be positive to ensure ferromagnetic alignment. The first term on the right is the Heisenberg exchange energy and the second is the Zeeman energy.
To make further progress we can use the Weiss model (14). In this model we define an effective molecular field $\overrightarrow{B}_{mf}$ and for a ferromagnet the molecular field will act so as to align neighboring magnetic moments. Since the molecular field measures the effect of the ordering of the system one can assume that

$$\overrightarrow{B}_{ef} = \lambda \overrightarrow{M} \tag{1.7}$$

where λ is a constant representing the strength of the molecular field. If we introduce external magnetic field $\overrightarrow{B}_e$ solving Hamiltonian 1.6 simplifies to solving Hamiltonian of paramagnet in magnetic field $\left(\overrightarrow{B}_{mf} + \overrightarrow{B}_e\right)$. The paramagnetic susceptibility will be

$$\chi_P = \frac{\mu_0 M}{(B_e + B_{mf})} = \frac{C}{T} \tag{1.8}$$

where C is Curie constant. If we substitute 1.7 in 1.8 we obtain

$$\chi = \frac{M}{\mu_0 B_e} = \frac{C}{T - C\lambda} = \frac{C}{T - T_C} \tag{1.9}$$

We can see that susceptibility has a singularity at $T = C\lambda = T_C$, which is for ferromagnet positive. This temperature is called Curie temperature and at this temperature spontaneous magnetization emerges. The last term in equation 1.9 is called $Curie - Weiss\ law$.

If the exchange interaction is negative ($J < 0$ in Hamiltonian 1.6) then nearest neighboring magnetic moments prefer to lie antiparallel to each other creating **antiferromagnetic** order. In most systems this can be considered as two interpenetrating lattices as shown in figure 1.3b. We can use linear dependence of magnetization on magnetic field 1.7 on each sublattice (the red and blue sublattice in figure 1.3b). The strength constant of the molecular field λ is negative for both sublattices. Applying the paramagnetic solution used for ferromagnet we obtain a relation for magnetic susceptibility (14)

$$\chi = \frac{2C}{T + T_N} \tag{1.10}$$

where C is Curie constant and T_N is Néel temperature below which spontaneous antiferromagnetic ordering occurs. Relations for susceptibilities of paramagnets,

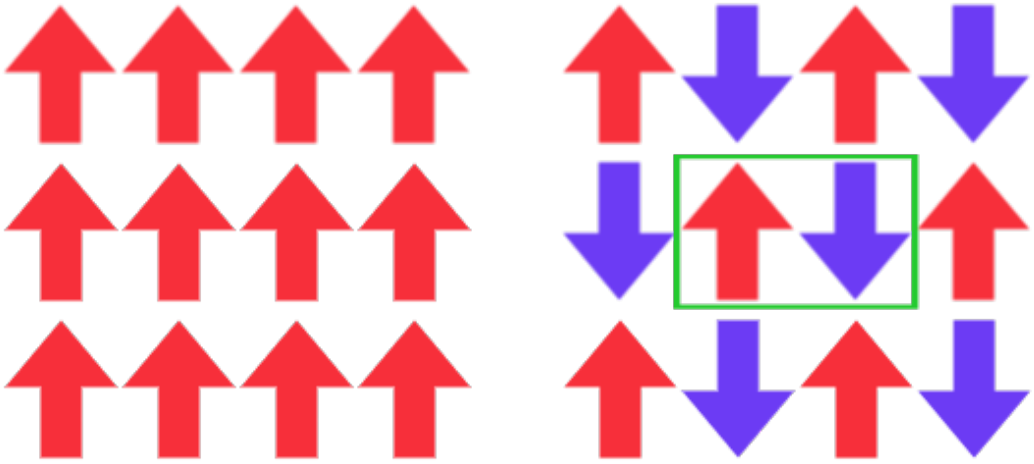

(a) Ferromagnetic ordering of magnetic moments

(b) Antiferromagnetic ordering of magnetic moments

Figure 1.3: The basic types of magnetic ordering. Arrows represent magnetic moments. (b) Purple and red color represent independent sublattices and green box indicates compensation of magnetic moments.

ferromagnets from equation 1.9 and antiferromagnets from equation 1.10 can be summarized with the general $Curie - Weiss\ law$

$$\chi = \frac{C}{T - \Theta_{cw}} \tag{1.11}$$

where Θ_{cw} is the paramagnetic Curie temperature (Weiss temperature) and C is Curie constant. From Weiss temperature we can determine the character of dominant interaction. For $\Theta_{cw} = 0$ material is paramagnet, for $\Theta_{cw} > 0$ we expect $\Theta_{cw} = T_C$ and it is ferromagnet and finally for $\Theta_{cw} < 0$ it is antiferromagnet with the predicted value $\Theta_{cw} = -T_N$.
The Curie constant C is directly related to the number of unpaired electrons and can be used to determine the effective magnetic moment per ion in the unit of Bohr magnetons (15)

$$\mu_{eff} = \sqrt{8C}\mu_B[\text{cgs}] \qquad \mu_{eff} \cong 800\sqrt{C}[SI] \tag{1.12}$$

Both of these equations relate effective magnetic moment to Curie constant with units (emu K mol^{-1}) in cgs and (m^3 K mol^{-1}). This effective moment can be directly compared to the calculated value for the ion in question, given by

$$\mu_{cal} = g_J\sqrt{J(J+1)}\mu_B \tag{1.13}$$

which depends only on its total angular momentum J and its g-tensor g_J. In $3d$ magnets the magnetic moment can be very well approximated by the spin-only moment and the equation 1.13 is reduced to (15)

$$\mu_{cal} = 2\sqrt{S(S+1)}\mu_B \tag{1.14}$$

In the previous paragraph we applied Weiss's mean field theory on ferromagnetic and antiferromagnetic structure. This model is a very powerful tool in magnetic data interpretation, but it breaks under certain circumstances for example in low temperatures because it does not reflects dynamics of the system. A more precise approach is by so-called **spin waves**. To introduce spin waves first imagine a chain of N spins with value S as shown in figure 1.4a). Energy associated with this chain is (16)

$$E_{ex} = -2JS^2(N-1) \tag{1.15}$$

where J is the strength of interaction between neighboring spins. Now suppose that we create an excitation, we flip one spin in the other direction as shown in figure 1.4b). Energy associated with this excited state is

$$E_{ex} = -2JS^2(N-3) + 2 \times 2JS^2 = -2JS^2(N-1) + 8JS^2 \tag{1.16}$$

So by flipping just one spin we created local excitation and increased energy of this system. When the spin flip is made gradually, the net increase in energy can be smaller. Thus a wave-like spin flip occurs, called spin wave and is shown in figure 1.4c).

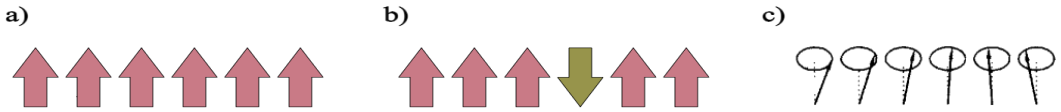

Figure 1.4: a) The classical picture of the ground state of a simple ferromagnet. b) A possible excitation: one spin is reversed. c) The low-lying elementary excitations, spin waves. The ends of the spin vectors press on the surfaces of cones, with successive spins advanced in phase by a constant angle (10).

A magnon is a quantized spin wave. Magnons as excitation have dispersion relations. The disperse relation for triangular lattice antiferromagnet with nearest neighbor interactions is (for calculation see appendix A)

$$E(\overrightarrow{k}) = 2JS\left(\cos k_x + 2\cos\frac{k_x}{2}\cos\frac{\sqrt{3}k_y}{2}\right) + B^* \tag{1.17}$$

where $\overrightarrow{k} = (k_x, k_y, k_z)$ is the propagation vector, J is the in-plane nearest neighbor interaction and $B^* = \Delta + g_L\mu B$, where B is external magnetic field, μ is magnetic moment of magnetic ion in the external field, g_L is the Landau g factor and Δ is the single-ion anisotropy.

1.3 Frustration

Some lattices do not allow to satisfy all the interactions in the system to find the ground state. This leads to multiple competing phases near the ground state. In that case we say that the system is frustrated. The antiferromagnet on the triangular lattice is shown in figure 1.5. This lattice shows frustration because it is not possible to orient the spin on the third site to satisfy the requirement of

antiferromagnetic interaction with two other spins.

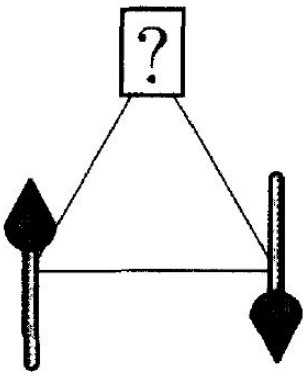

Figure 1.5: Antiferromagnetic nearest neighbor interaction on the triangular lattice. (10)

A possible experimental quantification of frustration is the so-called frustration ratio (17)

$$f = \frac{|\theta_{CW}|}{T_N} \tag{1.18}$$

where T_N is the ordering temperature (Neélé temperature) and Θ_{CW} is the Curie-Weiss temperature. Compounds with a frustration ratio greater than five are commonly called frustrated. The most extreme cases are materials without long-range order down to 0 K, meaning $f = \infty$, and correspond to a ground state with only short-range correlations. A regime with highly correlated but fluctuating spins and long-range order at temperatures $T \ll |\Theta_{CW}|$ is often titled "spin liquid" (more precise definitions are available in section 1.4.2).
A prime example of the frustrated system is a triangular lattice antiferromagnet. With an applied magnetic field, Heisenberg spins with isotropic exchange interactions exhibit a large ground-state degeneracy. That means that in a finite magnetic field, there exists an infinite number of continuously deformable spin configurations that constitute minimal energy states (18).
Considering Hamiltonian in equation 1.6 with nearest neighbor interaction can be simplified by considering the "side-sharing" property of the triangular lattice, so fixing all spins in one elementary triangle fixes two spins in each adjacent triangle. That implies that all such states exhibit a three-sublattice structure, which must satisfy (18)

$$S_1 + S_2 + S_3 = \frac{\mathbf{B}}{3J} \tag{1.19}$$

where S_i are spins on each apex of the triangle. This condition provides equations for angles needed to describe unit vectors defining the spins. In the absence of magnetic field three of these angles are in the plane and form a three-sublattice 120° structure and can persist to non-zero magnetic fields. One of the remaining free angles can be thought of as a gauge degree of freedom to rotate all spins about the axis of an applied magnetic field. Two other free angles constitute the phenomenon of accidental degeneracy.

Thermal fluctuations lift the extensive degeneracy in favor of two coplanar Y and V states and one collinear (UUD) spin configurations, shown in figure 1.6. Coplanar states break two symmetries, first is the symmetry corresponding to the choice of sublattice on which the down spin (in case of Y state) or the minority spin (in case of V state) is located and symmetry of spin rotation about the magnetic field axis. The collinear UUD state breaks only the choice of sublattice for the down spin (18). The UUD phase is also very easy to experimentally uncover. It shows as a plateau-like feature in magnetization curve M(B) at value M = $M_{sat}/3$, where M_{sat} is the saturated magnetization.

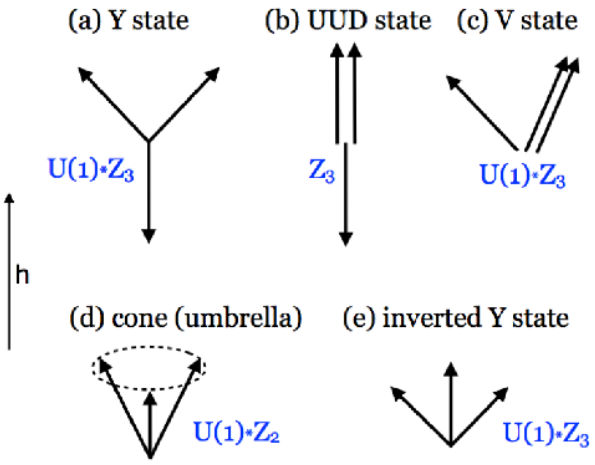

Figure 1.6: Various spin configurations from the ground state manifold. (a) coplanar Y state, (b) collinear UUD state, (c) coplanar V state, (d) non-coplanar cone state, (e) coplanar inverted Y state. Magnetic field **h** is directed vertically along z axis (18).

1.4 Spin liquid

An antiferromagnet consisting of a two-dimensional triangular lattice of Ising spins is one of the prime examples of a frustrated system, forming a very large degeneracy of ground states. At low temperatures spins continue to thermally fluctuate in a correlated manner because they are restricted by ground state, forming "spin liquid" (19). The name is analog to normal liquid, where molecules form dense, highly correlated state with no static order. The frustration parameter defined in equation 1.18 provides a measure of the depth of the spin-liquid regime.

Fluctuation of the spins in spin liquid can be classical or quantum. Classical fluctuations dominate for large spins and are driven by thermal fluctuations. Due to thermal fluctuations the spins reorient randomly with time and if thermal energy becomes too small classical fluctuations stop and spins freeze or order. For spins comparable to 1/2 the uncertainty principle produces motion of spins, which persists down to $T = 0$ K. Thermal (in the classical case) and quantum fluctuations are similar to each other, but quantum fluctuations can be phase coherent. If they are strong enough, they form a quantum spin liquid (QSL), which is a superposition state in which the spins simultaneously point in different directions. In a QSL, the spins are highly entangled with one another in a subtle way that

involves entanglement between widely separated spins (19).

1.4.1 Spin ice

Spin-ice materials can be regarded as classical spin liquids. Examples of such materials are $Dy_2Ti_2O_7$, $Ho_2Ti_2O_7$ and $Ho_2Sn_2O_7$ (20), where only ions of rare-earth atoms (Dy and Ho) are magnetic and resides on a pyrochlore lattice, which is a network of corner-sharing tetrahedra. Their f-electron spins are large and classical and their mutual nearest neighbor interactions are ferromagnetic, resulting in frustration. To minimize the energy of a single tetrahedron spins have to align into a configuration in which two spins point inward and two spins point outward from the center of the tetrahedron (see figure 1.7). The name spin ice originates from a direct analogy between these configurations and the positions of protons in the tetrahedrally coordinated O^{2-} framework of water ice (21).

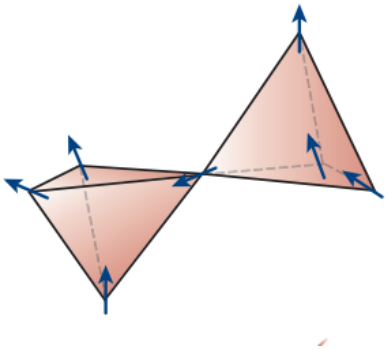

Figure 1.7: A ground-state configuration of spins is shown in a pyrochlore lattice. The spins obey the constraint of the ice rules that mandates two inward-pointing spins and two outward-pointing ones on each tetrahedron (19).

1.4.2 Quantum spin liquid

In spin ice with decreasing temperature spin fluctuation decreases and eventually falls out of equilibrium and freezes. This is the consequence of the large energy barriers between different ice-rule configurations (22). By contrast, for materials with spins of $S = 1/2$ quantum effects are strong and there are no obvious energy barriers.
The most basic building block for a non-magnetic state is a valence bond, which is a pair of spins forming a spin-0 singlet state shown in figure 1.8a. A valence bond is a highly quantum object, where the two spins are maximally entangled. To build quantum spin liquid valence bond must be allowed to undergo quantum mechanical fluctuations. The ground state is then a superposition of different partitioning of spins into valence bonds. Not all quantum spin liquids are alike. The valence bond does not have to form only for nearby spins. If a valence bond is formed for distant spins, then the bond is weak and can be broken forming free spin with low energy. So states that have a significant weight from long-range valence bonds have more low-energy spin excitations than states in which the

valence bonds are mainly short-range (19).

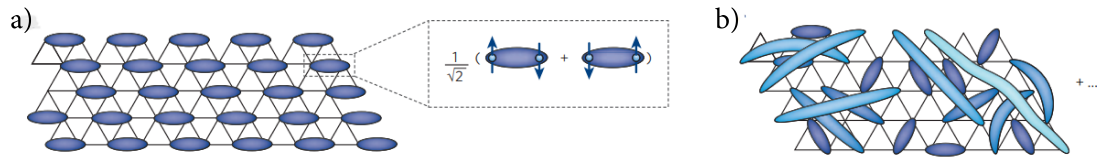

Figure 1.8: In a VBS state a), a specific pattern of entangled pairs of spins — the valence bonds - is formed. Entangled pairs are indicated by ovals that cover two points on the triangular lattice. b) Spins in longer-range valence bonds (the longer, the lighter the colour) are less tightly bound and are therefore more easily excited into a state with non-zero spin (19).

In quantum spin liquids, there is one feature connecting them all, these are exotic excitations. These exotic excitations are spinons, which are neutral and carry spin 1/2. If we consider one-dimensional system, then spinons occur as domain walls (see figure 1.9a) between spin up string and spin down string. In true two-dimensional and three-dimensional quantum spin liquids the spinon can be understood as a quantum superposition of reshuffled various spins and valence-bond configuration that are already superposed in the ground state (19) (see figure 1.9b).

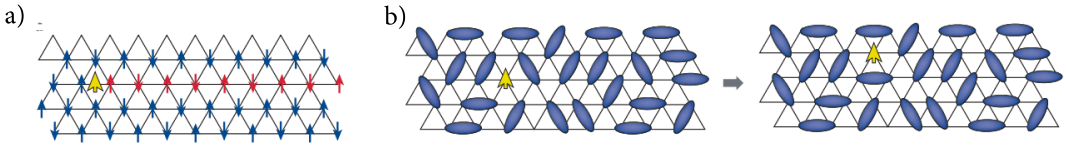

Figure 1.9: a) In a quasi-1D system (such as the triangular lattice depicted), 1D spinons are formed as a domain wall between the two antiferromagnetic ground states. Creating a spinon (yellow arrow) thus requires the flipping of a semi-infinite line of spins along a chain, shown in red. b) In a 2D QSL, a spinon is created simply as an unpaired spin, which can then move by locally adjusting the valence bonds (19).

1.5 Neutron scattering

A neutron is a charge-neutral particle that deeply penetrates matter, making it the perfect probe for bulk measurements of various condensed matter phenomena. A particle with kinetic energy E and momentum p has according to the de Broglie and Planc-Einstein equations wavelength λ and frequency ν

$$p = \frac{h}{\lambda} = \hbar k \tag{1.20}$$

$$E = h\nu \tag{1.21}$$

where $h = 6.626{\cdot}10^{-34}$J is the Planck constant, $\hbar = h/2\pi$ the reduced Planck constant, and $k = 2\pi/\lambda$ the wavevector (23).
Scattering as an interaction of neutron and nuclei is depicted in figure 1.10. A neutron with initial energy E_i and wavevector k_i is scattered into final state with energy E_f and k_f

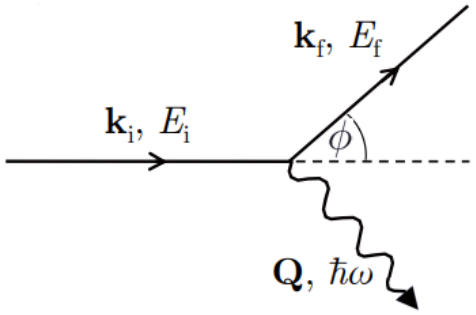

Figure 1.10: Reprezenattion of scattering event (24)

The vector $\mathbf{Q} = \mathbf{k}_i$ **-** $\mathbf{k}_f$ is called the scattering vector and the energy deposited into the sample during the scattering event is defined as $\hbar\omega = E_i - E_f$. Elastic scattering is defined by zero energy transfer during scattering event $E_i = E_f$ and during inelastic scattering the energy changes $E_i \neq E_f$.
We can express scattering event as cross-section. Total scattering cross-section measures the likelihood of neutron being scattered by the target normalized by an incoming flux of neutrons. However, during experiment we want to measure a number of neutrons scattered in some general direction. We than define differential scattering cross-section as the number of neutrons scattered into angle $d\Omega$. For fixed nuclei in elastic neutron scattering the differential cross-section is defined as

$$\frac{d\sigma}{d\Omega} = |\sum_j b_j \exp(iQ \cdot r_j)|^2 \tag{1.22}$$

where b_j is scattering length and r_j position of said nuclei. When measuring inelastic scattering we define a partial differential cross-section $\frac{d^2\sigma}{d\Omega dE_f}$ as differential cross-section but the energies of scattered neutrons have to be in the interval $(E_f, E_f + dE_f)$.
Neutrons as particles possess magnetic moment of 1.9 μ_N ($\mu_N = 5.005{\cdot}10^{-27}$ Am^{-1} is nuclear magneton) and spin 1/2 which makes it the perfect probe for studying magnetism in condensed matter. Neutrons interact with microscopic electromagnetic fields through electromagnetic interactions, which are much weaker and their range is much longer. The differential cross- section is given by Fermi's golden rule

$$\frac{d^2\sigma_{k_i \to k_f}}{d\Omega dE_f} = \frac{k_f}{k_i}\left(\frac{m_n}{2\pi\hbar^2}\right)^2 \sum_{\lambda_i} p_{\lambda_i} \sum_{\lambda_f} |\langle \sigma_f \lambda_f | V(\mathbf{Q}) | \sigma_i \lambda_i \rangle|^2 \delta(E_{\lambda_f} - E_i - \hbar\omega) \tag{1.23}$$

where V($\mathbf{Q}$) is the Fourier transform of the interaction potential between neutron and scattering system. Labels λ_i, λ_f and σ_i, σ_f represent state of neutron and

system before and after the interaction. For magnetic materials, we can separate the nuclear and magnetic part of V($\mathbf{Q}$)

$$V(\mathbf{Q}) = V_N(\mathbf{Q}) + V_M(\mathbf{Q}) \tag{1.24}$$

where magnetic potential is

$$V_M(\mathbf{Q}) = -\mu_0\mu_B \cdot \mathbf{M}_\perp(\mathbf{Q}) \tag{1.25}$$

where $\mathbf{M}_\perp(\mathbf{Q})$ is the Fourier transform of the corresponding magnetization, which is perpendicular to the scattering vector. By combining equations 1.23 and 1.25 we obtain magnetic scattering cross-section

$$\frac{d^2\sigma_{k_i \to k_f}}{d\Omega dE_f} = \frac{k_f}{k_i}\left(\frac{\gamma r_0}{2\mu_B}\right)^2 S(\mathbf{Q},\omega) \tag{1.26}$$

where $\gamma = 1.913$, $r_0 = \mu_0 e^2/(4\pi m_e) = 2.818 \cdot 10^{-15}$ m, and

$$S(\mathbf{Q},\omega) = \sum_{\lambda_i} p_{\lambda_i} \sum_{\lambda_f} |2\langle\sigma_f|s_n|\sigma_i\rangle \cdot \langle\lambda_f|\mathbf{M}_\perp(\mathbf{Q})|\lambda_i\rangle|^2 \delta(E_{\lambda_f} - E_i - \hbar\omega) \tag{1.27}$$

is the magnetic response function.

1.5.1 Propagation vector

Let us return to the magnetic structure introduced in section 1.2.2. It is important to stress the difference between magnetic unit cell and a nuclear unit cell. The magnetic unit cell is the smallest unit that has the same magnetic surroundings. The magnetic unit cell is always greater or the same as the nuclear unit cell. If the magnetic and crystal lattice periods are related by an integer or a rational fraction then the magnetic structure is commensurate with the crystal lattice. A magnetic unit cell cannot be defined if the periodicity of the magnetic structure is not commensurate with the chemical lattice. Such structures are said to be incommensurate. The relationship between magnetic and nuclear unit cell is described by propagation vector, which is defined as one over number of nuclear unit cells in one magnetic unit cell in certain direction.

2 Studied Materials state of arts

2.1 $Na_2BaM(PO_4)_2$ (M = Co, Ni, Mn)

Materials with formula $Na_2BaM(PO_4)_2$ (M = Co, Mn, Ni) are currently under active study, both theoretically and experimentally, because they exhibit rich magnetic phase diagrams at low temperatures due to complex magnetic interactions and strong quantum fluctuations of the magnetic moment. They are promising candidates for a quantum spin liquid state. $Na_2BaCo(PO_4)_2$ (25) and $Na_2BaMn(PO_4)_2$ (8) have trigonal crystal structure shown in Fig. 2.1. $Na_2BaNi(PO_4)_2$ was first reported as space group $P\bar{3}$ (26), but most recent study suggest the same structure as Co and Mn compounds (27).
Structural and magnetic properties of compounds with common formula $Na_2BaM(PO_4)_2$ are summed up in table 1.

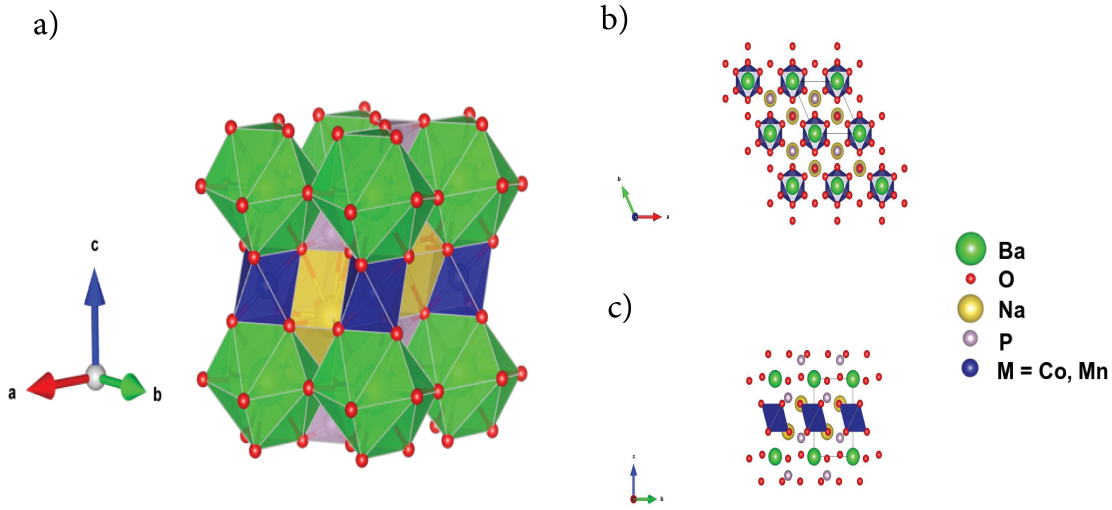

Figure 2.1: The structure of $Na_2BaM(PO_4)_2$. **a)** The crystal structure of $Na_2BaM(PO_4)_2$ based on the packing of M-O polyhedra. **b)** Top view of the relative orientation of the MO_6 and other groups in the 2D triangular layer. **c)** View emphasizing the layers of MO_6 octahedra along the c axis view from the b axis.(25)

Formula	Space group	$a(\AA)$	$c(\AA)$	$V(\AA^3)$	S(spin)	T_N (K)
$Na_2BaCo(PO_4)_2$	$P\bar{3}m1$	5.3185	7.0081	171.676	1/2	0.15
$Na_2BaNi(PO_4)_2$	$P\bar{3}/P\bar{3}m1$	5.2790	6.9596	167.96	1	0.41
$Na_2BaMn(PO_4)_2$	$P\bar{3}m1$	5.3761	7.0999	177.38	5/2	1.32

Table 1: Summarizing of the most important magnetic properties of $Na_2BaM(PO_4)_2$ (25; 26; 8)

Single crystal diffraction on these compounds (25; 26; 8) indicates that the compounds are stoichiometric with a simple whole number ratio of constituents.

Schematic diagrams of their crystal structure are shown in figure 2.1. Triangular layers of magnetic MO_6 octahedra form A-A-A stacking pattern. The magnetic layers are separated by a single layer of nonmagnetic BaO_{12} polyhedra with $[PO_4]^{3-}$ units and Na^+ filling the gaps in the magnetic layers. The magnetic exchange coupling of magnetic octahedra depends on the overlap of metal-oxygen and oxygen-oxygen bonds (superexchange). This means that the coupling in the same triangular layer is trough M-O-O-M (M = Co, Ni, Mn) super-superexchange (J_1) and the exchange coupling of neighboring layers is trough M-O-O-O-M super-super-superexchange (J_2). This situation is shown in figure 2.2. In these compounds, the in-plane exchange J_1 is much larger than the exchange between planes J_2, which makes these compounds effectively 2-dimensional triangular magnets.

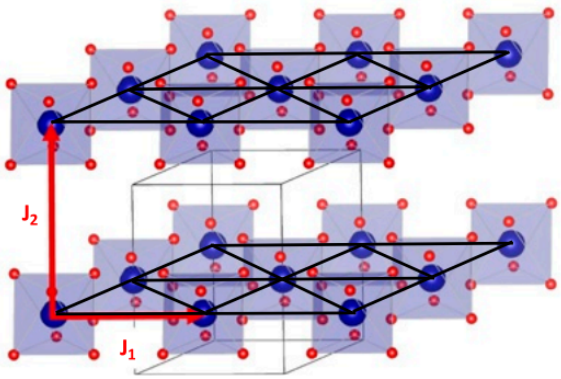

Figure 2.2: The triangular layer of MO_6 octahedra in the *ab* plane, with J_1 and J_2 marked to indicate the super-exchange coupling between the nearest neighbor M ions in the same plane and the neighboring plane. (25)

2.1.1 $Na_2BaCo(PO_4)_2$

Quantum spin liquid candidate $Na_2BaCo(PO_4)_2$ has Co^{2+} with effective spin S=1/2 residing on a geometrically frustrated triangular lattice. A significant advantage of this material is that it does not display any significant site mixing or lattice distortion and is simply growable.
The Curie-Weiss law was applied to fit the susceptibility from 200 to 300 K, measured in fig 2.3. From the fit was found $\Theta_{CW,\perp}$ = -31.9 K, $\mu_{eff,\perp}$ = 4.96 μ_B and $\Theta_{CW,\parallel}$ = -32.6 K, $\mu_{eff,\parallel}$ = 5.87 μ_B for the magnetic field applied perpendicular and parallel to the c axis respectively, indicating that the antiferromagnetic interaction dominate.

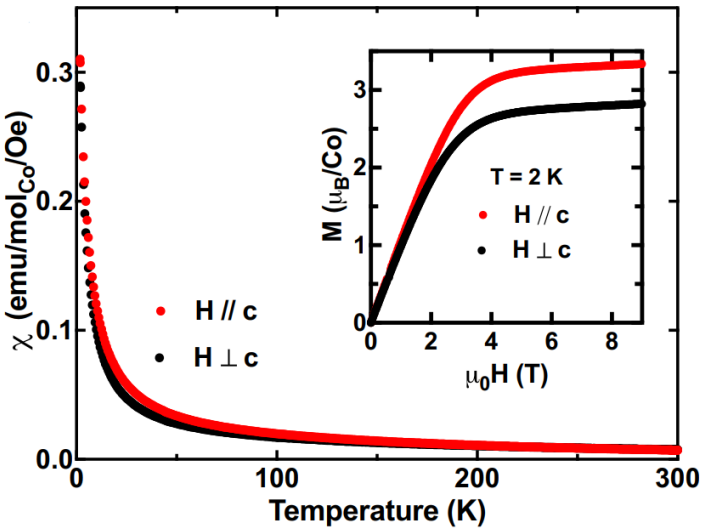

Figure 2.3: Temperature dependence of *dc* susceptibility down to 1.8K measured with $\mu_0 H = 0.1$T on a single crystal sample oriented with external field perpendicular to c axis (H$\perp c$; black) and parallel to the c axis (H$\|c$; red) (25)

For this compound magnetic phase diagram has been reported (6). To construct this phase diagram thermal conductivity, specific heat and AC susceptibility have been measured. The magnetic phase diagram is in figure 2.6 for directions $B\|c$ and $B\perp c$. For $B\|c$ it is clear that the phase II is up up down (UUD) phase, which is deduced from the $1/3M_s$ plateau in magnetization measurement observed at 22mK, which is shown in Fig. 2.4a. Since the 120° spin structure is a prerequisite phase for the appearance of the UUD phase, we ascribe the phase I as the canted 120° spin structure. For the H$\perp c$ the UUD phase was not observed as shown in Fig. 2.4b.

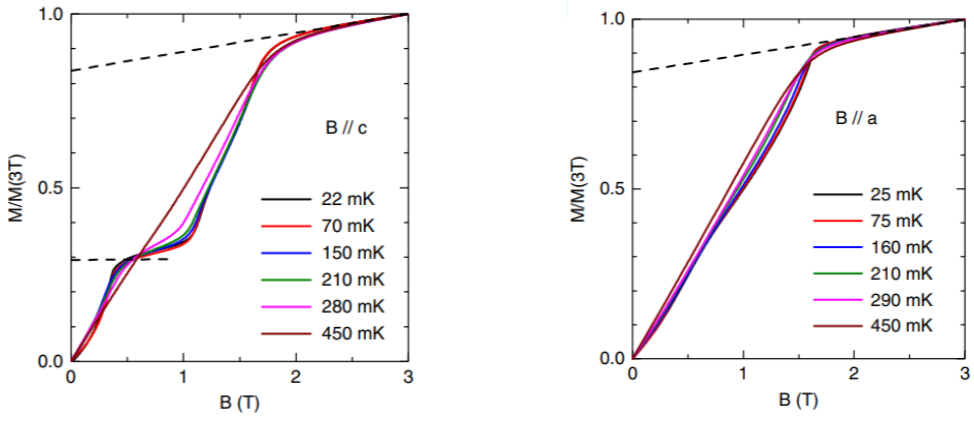

Figure 2.4: Measurement of magnetisation dependence on the magnetic field. The top dashed line indicates saturated magnetization. **a)** Magnetization curve with magnetic field applied along c axis The lower dashed line indicates a 1/3 plateau. **b)** Magnetization curve with magnetic field applied along a axis (6).

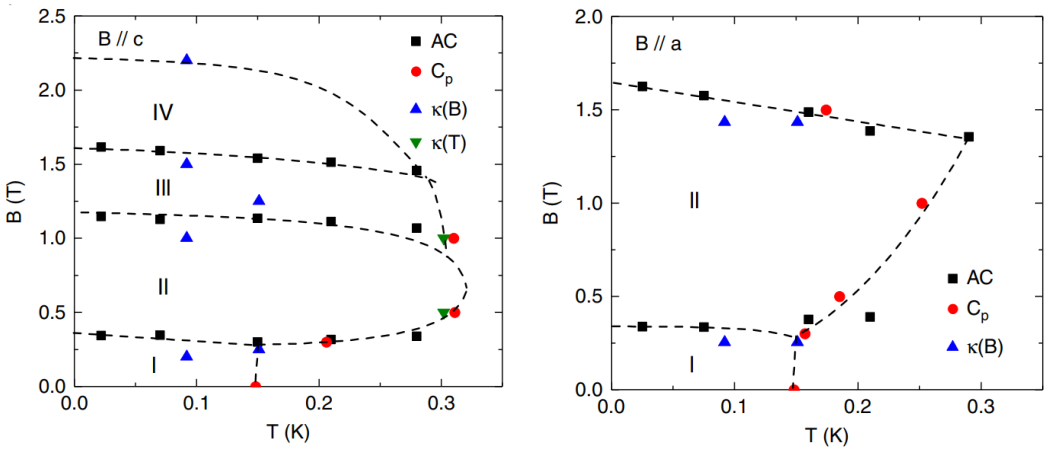

(a) (b)

Figure 2.5: The magnetic phase diagram of $Na_2BaCo(PO_4)_2$ for B$\|c$ (**a**) and B$\perp c$ (**b**). The data points are obtained from the AC susceptibility (AC), specific heat (C_p) and temperature or field dependence of thermal conductivity (κ(T) and κ(B)) measurements. The dashed lines are to guide the eye. (6)

The single crystal neutron diffraction experiments on a $Na_2BaCo(PO_4)_2$ were performed (28). The magnetic Bragg peaks were observed at 50 mK (see figure 2.6a). All observed magnetic reflections can be indexed by propagation vector $\overrightarrow{k} = (1/3, 1/3, \pm 0.167(3))$.
The spin wave dispersion in a fully polarized state (B = 3.5 T) measured along points M-K-Γ_1-M in figure 2.6b. The energy gap around 0.484(5) meV arose at K point. Empty circles are the fitted center position and the solid blue line is the simulated linear spin wave dispersion by equation 1.17 and the coefficients are J = 0.076(1) meV and B^* = 0.128(9) meV.

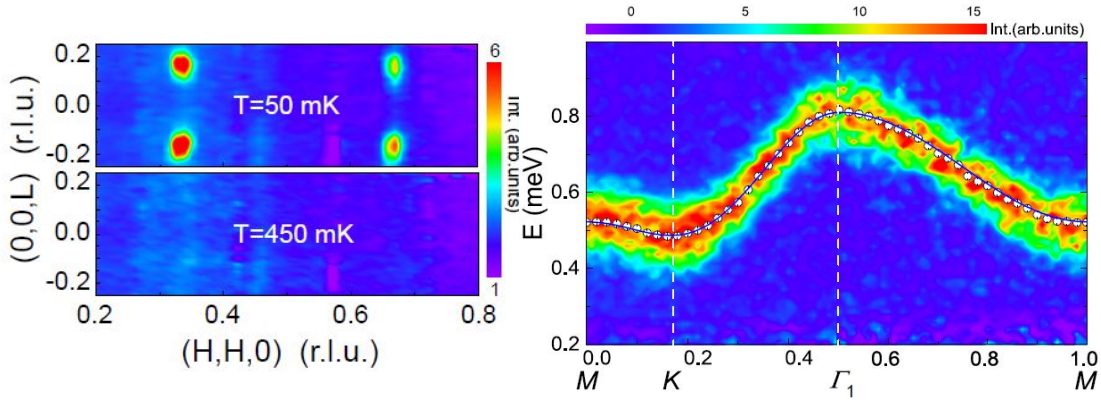

(a) (b)

Figure 2.6: a) Magnetic Bragg peaks at temperature 50 mK that disappear at temperature 450 mK. b) Contour maps of the experimental spin wave dispersion along M-K-Γ_1-M direction in the fully polarized state, in field B = 3.5 T and at temperature T = 50 mK (28).

2.1.2 $Na_2BaNi(PO_4)_2$

DC susceptibility was measured on single crystal from 2 K to 300 K and Curie-Weiss law was applied on data between 50 K and 300 K shown in figure 2.7. The fitting results are $\Theta_{CW,\parallel} = -6.615$ K and $\mu_{eff,\parallel} = 3.092\mu_B$ and $\Theta_{CW,\perp} = -43.979$ K, $\mu_{eff,\perp} = 3.832\mu_B$ for $\chi_\parallel(T)$ and $\chi_\perp(T)$ respectively. The significant difference between $\Theta_{CW,\parallel}$ and $\Theta_{CW,\perp}$ reveals strong magnetic anisotropy.

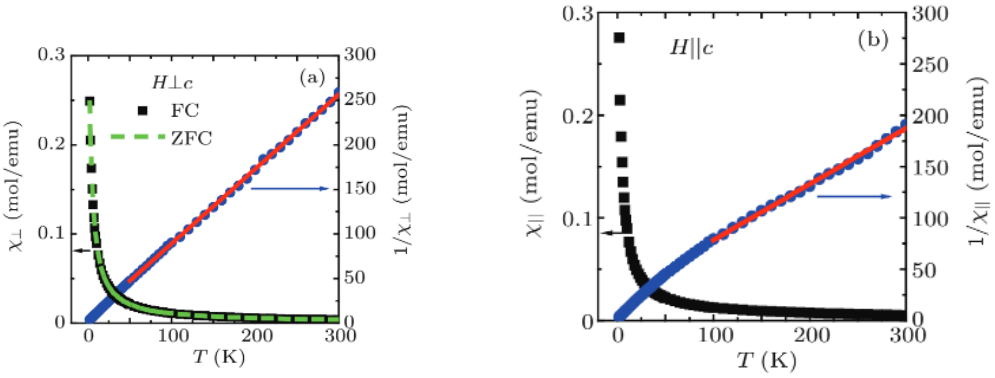

Figure 2.7: Magnetic susceptibility with field applied **a)** parallel and **b)** perpendicular to c. The FC data (clack squares) and ZFC data (green dashed line) were measured under H = 1 T and in the temperature range 2K to 300 K. The red solid line are the Curie-Weiss law fitting for the $1/\chi$ data (blue dots) (26)

To further reveal the magnetic anisotropy magnetization at T = 300 K, 100 K, 50 K, 2 K with magnetic field parallel or perpendicular to c axis was measured, the results are shown in figure 2.8.

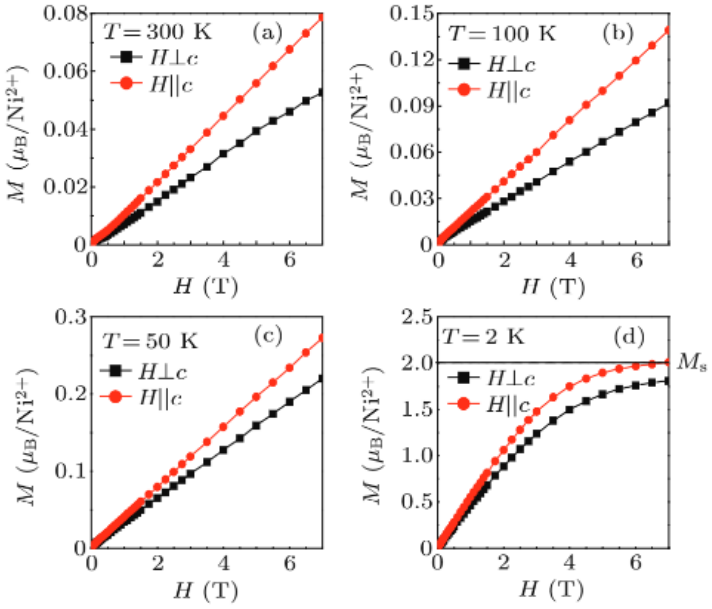

Figure 2.8: Magnetization of $Na_2BaNi(PO_4)_2$ at **a)** 300 K, **b)** 100 K, **c)** 50 K and **d)** 2 K. The dotted line in **d)** indicates the saturated magnetization value for a Ni^{2+} ion when only concerning the spin moment. (26)

In figure 2.8(a)-2.8(c) both $M_{\parallel}$ and $M_{\perp}$ increase linearly from 0 to 7 T with $M_{\parallel}$ larger than $M_{\perp}$. The anisotropy can be observed at 300 K, indicating the anistropic excitation gap should be comparable with the thermal energy. At 2 K M is proportional to H at lower fields and tends to saturate at higher fields. Saturation magnetization equals to 2 μ_B/Ni^{2+}. The magnetization curves at all measured temperatures have no anomaly, indicating the absence of magnetic transition or long-range order.
To construct a magnetic phase diagram of $Na_2BaNi(PO_4)_2$ the temperature dependence of specific heat C_p(T), magnetic field and temperature dependence of ac susceptibility χ'(B), χ'(T) and magnetic field and temperature dependence of thermal conductivity κ(B), κ(T) were measured and the final phase diagram is in figure 2.9(a,b). The UUD phase was recognized as phase II along c axis. This phase was discovered by magnetization 1/3 plateau in figure 2.9(c,d).

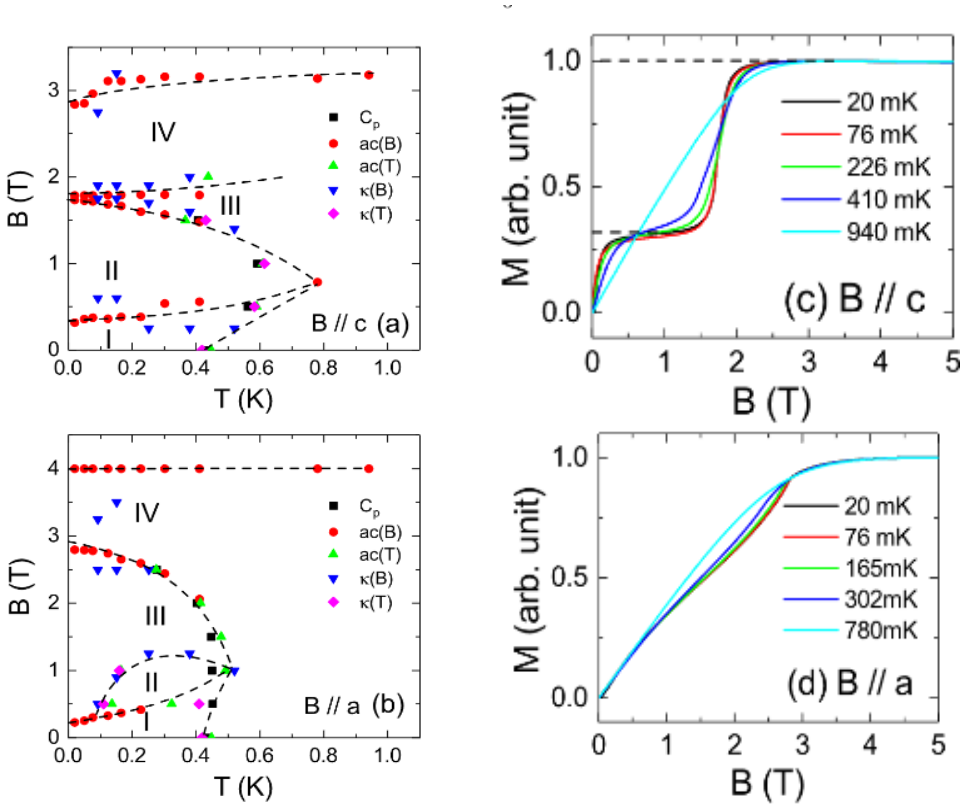

Figure 2.9: The magnetic phase diagram of $Na_2BaNi(PO_4)_2$ with field applied along the c axis (a) and ab plane (b). Magnetization along c axis (c) and a axis (d) obtained by integrating the AC susceptibility curve. (7)

Single crystal neutron scattering experiment on $Na_2BaNi(PO_4)_2$ was performed at zero field and a low temperature T = 80 mK shown in figure 2.10. All observed magnetic reflections can be classified by propagation vector equivalent to $\mathbf{k} = (1/3, 1/3, \pm\delta)$ where $\delta \approx 0.293(1)$.
The spin wave dispersion in fully polarized state (B = 5 T) was measured along points Γ_1-K-M-Γ. The black empty circles are centers of the Gaussian fit to the data. These points were fitted by equation 1.17 and coefficients J = 0.032(1) meV and B^* = -0.090(1) meV.

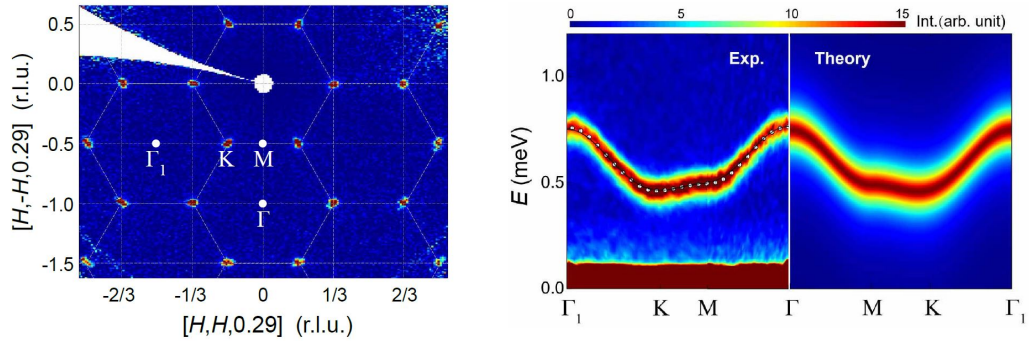

(a)

Figure 2.10: a) The neutron diffraction pattern measured in the L = 0.29 plane at T = 80 mK and B = 0T. b) Inelastic neutron scattering intensity measured at T = 60mK and B = 5T along Γ_1-K-M-Γ. (27)

2.1.3 $Na_2BaMn(PO_4)_2$

$Na_2BaMn(PO_4)_2$ was first found in Japan as a naturally grown crystal found in Japan called Iwatite (29).
Temperature dependence of DC magnetic susceptibility was measured and is shown in figure 2.11a. The χ(T) curves show a monotonic increase upon cooling from 320 to 1.8 K without any significant long-range order. Using the Curie-Weiss model at 20K$\leq$ T $\leq$ 100 K the Curie-Weiss temperature $\Theta_{CW,\perp}$ = -7.20 K and $\Theta_{CW,\parallel}$ = -7.61 K and effective magnetic moment $\mu_{eff,\perp}$ = 5.61 μ_B and $\mu_{eff,\parallel}$ = 5.60 μ_B on one Mn ion were found (8). Magnetization measurement, shown in figure 2.11b, was performed at temperature 2 K. It shows isotropic behavior in both directions. The slope changes around 6 T, but it does not saturate up to the maximum magnetic field measured.

For the construction of the magnetic phase diagram, the temperature depen-

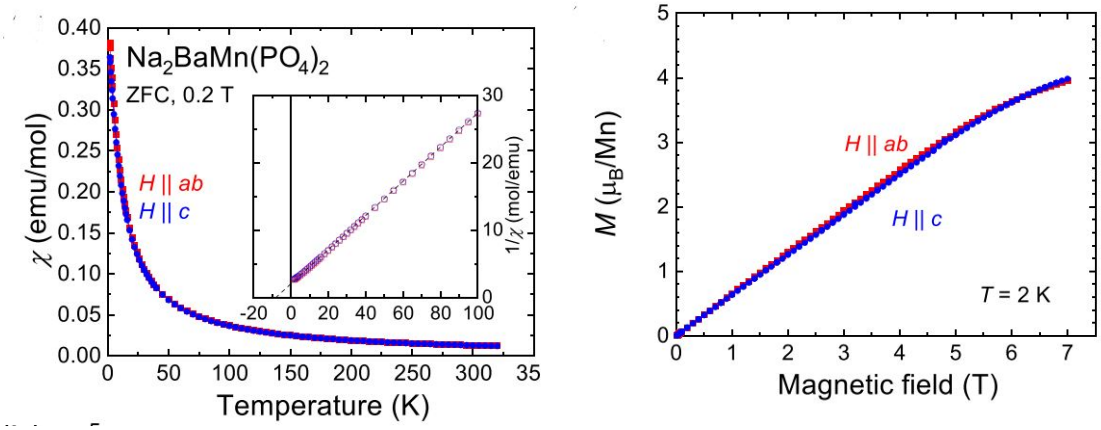

(a) (b)

Figure 2.11: **a)** Temperature dependence of susceptibility measured along two crystallographic orientations. **b)** Magnetic field dependence of magnetization at 2K. (8)

dence of specific heat was measured in the temperature range 0 K to 2 K in a different magnetic field in the range from 0 T to 4 T in two directions $H \parallel c$ and $H \parallel ab$. To further track the magnetic transitions both temperature and field-dependent AC magnetic susceptibility was measured. The field-dependent AC susceptibility was measured in a range from 0 T to 7 T and also from 7 T to 0 T. Strong hysteresis of AC susceptibility along the c axis was observed around 3 T and the hysteresis weakens with increasing temperature (see figure 2.12a). Combining C_p(T), χ(T), and χ(H) data the full magnetic phase diagram of $Na_2BaMn(PO_4)_2$ along two applied field directions was obtained and is shown in figure 2.12(a,b). When the magnetic field is applied along the c axis we observe a series of ordered phases. Only the UUD phase can be determined by magnetization plateau at $1/3M_s$, which is shown in figure 2.12c. When the field is applied along the ab plane the phase diagram consists of three phases. The UUD phase is absent, which suggests easy-axis anisotropy of this system.

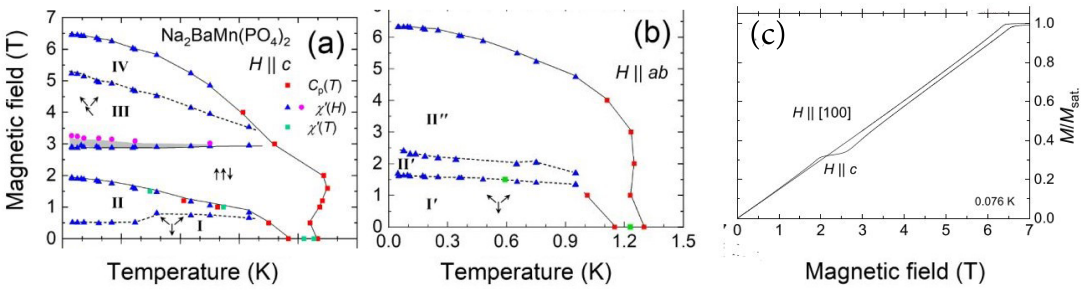

Figure 2.12: The magnetic phase diagram of $Na_2BaMn(PO_4)_2$ with field applied along the c axis (a) and ab plane (b). Grey area in (a) describes the hump region with hysteresis observed in AC susceptibility. (c) Magnetization along two directions at 0.076K obtained by integrating the AC susceptibility curve(8).

2.2 $Na_2BaM(VO_4)_2$ (M = Co, Ni, Mn)

Compounds $Na_2BaM(VO_4)_2$ (M = Co, Mn, Ni) are new series of triangular lattice magnets. Their structure has been reported to be $P\bar{3}$ (30) and $P\bar{3}m1$ (31). Making their structure very similar to $Na_2BaM(PO_4)_2$ (M = Co, Mn, Ni) shown in figure 2.1. The magnetic MO_6 (M = Co, Ni, Mn) octahedra is separated by VO_4 tetrahedral instead of PO_4. The lattice constants of the three materials are $a = 5.5223(3)\AA$ and $c = 7.0419(5)\AA$ (M=Ni), $a = 5.54880(10)\AA$ and $c = 7.0730(2)\AA$ (M = Co) and $a = 5.5962(3)\AA$ and $c = 7.1653(4)\AA$ (M = Mn).

2.2.1 $Na_2BaCo(VO_4)_2$

Magnetic susceptibility of $Na_2BaCo(VO_4)_2$ was measured in temperature range 2 K to 300 K. Curie-Weiss law fitting was performed on the data between 200 K and 300 K (see figure 2.13a) which give us $\Theta_{CW,\parallel} = 13$ K and $\mu_{eff,\parallel} = 5.865\mu_B$ and $\Theta_{CW,\perp} = -54$ K and $\mu_{eff,\perp} = 5.585\mu_B$. However if we fit data in temperature

region 5 to 25 K (see figure 2.13a) we obtain $\Theta_{CW,\parallel} = 3.1$ K and $\mu_{eff,\parallel} = 5.441\mu_B$ and $\Theta_{CW,\perp} = 1.7$ K and $\mu_{eff,\perp} = 3.687\mu_B$. This difference is caused by considerable contribution from the orbital moment. A magnetic phase transition is observed at $T_C = 3.9$ K.
Figure 2.13b shows magnetization curve measured at 2 K.

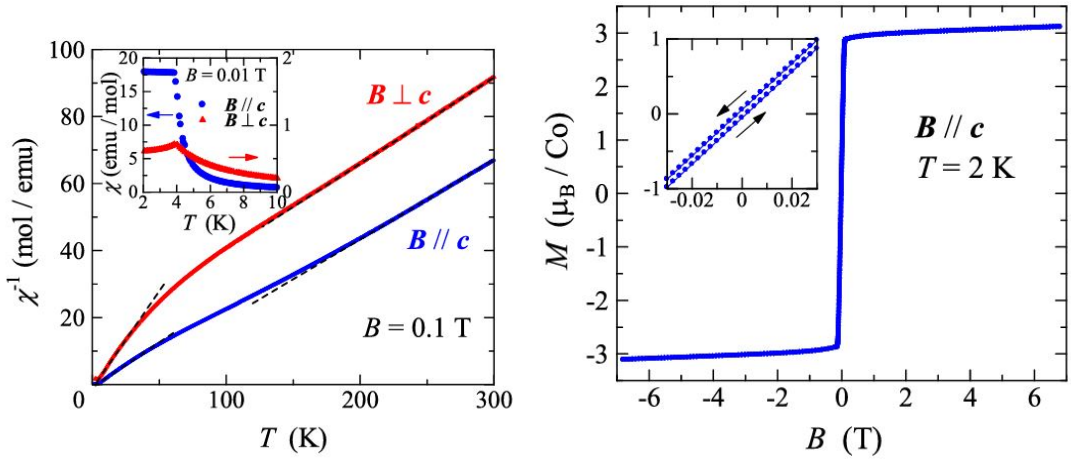

(a) (b)

Figure 2.13: **a)** Reciprocal magnetic susceptibility of $Na_2BaCo(VO_4)_2$ from 1.8 and 300 K. The dashed lines show the results of Curie–Weiss fitting. The inset shows the magnetic susceptibility at low temperatures. **b)** Magnetization curve of $Na_2BaCo(VO_4)_2$ measured at 2K under magnetic fields along the c axis. The inset shows the detail in the low-field region. (30)

2.2.2 $Na_2BaNi(VO_4)_2$

Figure 2.14a shows the reciprocal magnetic susceptibilities of $Na_2BaNi(VO_4)_2$ as a function of temperature measured under the two directions of a magnetic field. Overall, the results seem to be linear over the temperature range measured. The susceptibility is slightly anisotropic over the entire temperature region, which can be attributed to the anisotropy of the g value due to spin–orbit coupling. A Curie–Weiss analysis of the data for 100–300 K (see figure 2.14a) gives a $\Theta_{CW,\parallel} = 3.6$ K and $\mu_{eff,\parallel} = 3.464\mu_B$ and $\Theta_{CW,\perp} = 6.5$ K and $\mu_{eff,\perp} = 3.225\mu_B$. The positive Weiss temperature indicates that the nearest neighbor exchange interactions are ferromagnetic. The inset of figure 2.14a shows that this compound undergoes a magnetic phase transition at T_C 8.4 K. The magnetic susceptibility for the in-plane magnetic field rises steeply at around T_C, while that for the out-of-plane field has a sharp bend at T_C.
Figure 2.14b shows the magnetization curves measured at 2 K. For $B \perp c$, the magnetization rises steeply with the magnetic field and becomes almost saturated at 0.1 T. The magnetization curve for $B \parallel c$ with low magnetic fields shown in the inset has a slight hysteresis. In contrast, the magnetization is less sensitive to the $B \parallel c$ fields, where no hysteresis or spontaneous magnetization is observed in the magnetization curves. The magnetization saturation values are 2.3 and 2.2 μ_B for $B \parallel c$ and $B \perp c$ respectively.

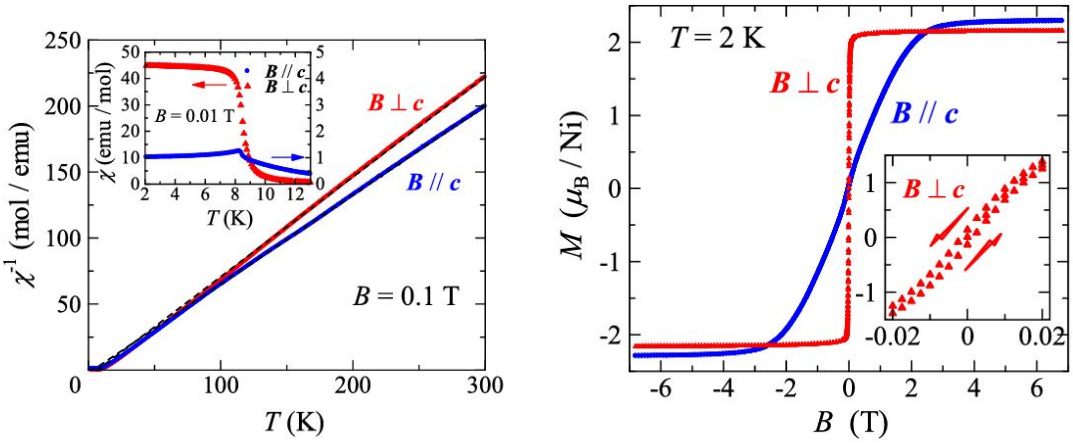

(a) (b)

Figure 2.14: **a)** Reciprocal magnetic susceptibility of $Na_2BaNi(VO_2)_4$ from 1.8 and 300 K.The dashed line shows the result of Curie–Weiss fitting. The inset shows the magnetic susceptibility at low temperatures. **b)** Magnetization curves of $Na_2BaNi(VO_4)_2$ measured at 2K. The inset shows the detail under low magnetic fields perpendicular to the c axis.(30)

2.2.3 $Na_2BaMn(VO_4)_2$

Figure 2.15a shows the reciprocal magnetic susceptibility of $Na_2BaMn(VO_4)_2$ measured in the temperature range 2 to 300 K. Although the reciprocal susceptibilities are linear in wide range of temperature, the Currie-Weiss fit was performed between 100 and 300 K. The fits give us $\Theta_{cw,\perp} = -4.5$ K and $\mu_{eff,\perp} = 5.865\mu_B$ and $\Theta_{cw,\parallel=-9.4}$ K and $\mu_{eff,\parallel} = 6.131\mu_B$. The negative Weiss temperatures indicate that the nearest-neighbor exchange interactions are antiferromagnetic in this material. Therefore, the effect of geometric frustration arising from the triangular arrangement of the magnetic atoms can be expected.
Figure 2.15b shows the magnetization curves for $Na_2BaMn(VO_4)_2$ under magnetic fields parallel and perpendicular to the c axis. The top-left inset of figure 2.15b shows that the magnetization curve measured at 2 K is slightly anisotropic, which is qualitatively in accordance with the anisotropy indicated from the g value. The magnetization increases almost proportionally to the magnetic field up to 4 T and then curves gently downward at higher magnetic fields without any anomalies that would indicate a phase transition. This behavior suggests that $Na_2BaMn(VO_4)_2$ is still in a paramagnetic state at 2 K. At 0.6 K, the magnetizations under both directions of the magnetic field reach saturation at approximately 6 T, where a sharp bend appears.

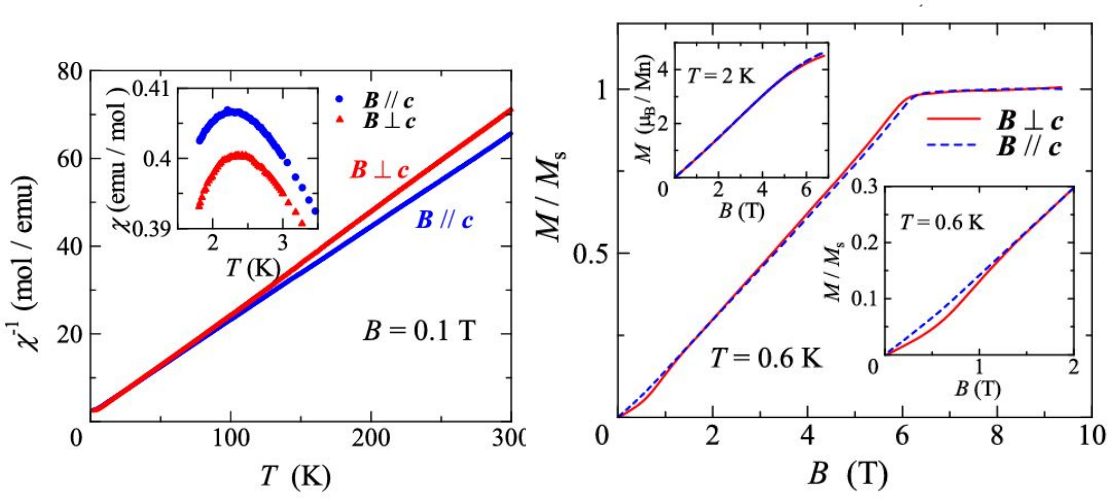

(a) (b)

Figure 2.15: **a)** Reciprocal magnetic susceptibility of $Na_2BaMn(VO_4)_2$ from 1.8 and 300 K. The inset shows the magnetic susceptibility at low temperatures. **b)** Magnetization curves of $Na_2BaMn(VO_4)_2$ measured using a pulse magnet at 0.6 K. The bottom-right inset shows the detail at low magnetic fields. The top-left inset shows the magnetization curves measured using the SQUID at 2 K. The magnetizations at 0.6 K are normalized according to the saturation values. (30)

2.3 Selection of studied material

All of the materials described in section 2 were considered as possible candidates for our neutron experiment. Isostructural $Na_2BaCo(PO_4)_2$ and $Na_2BaNi(PO_4)_2$ are very good spin liquid candidates (6; 7) with low spin value, but neutron experiments have already been performed on these compounds (28; 27).
Compounds $Na_2BaCo(VO_4)_2$ and $Na_2BaNi(VO_4)_2$ are not suitable for studying quantum spin liquid behavior because they exhibit ferromagnetic interactions.
Even thought $Na_2BaMn(VO_4)_2$ exhibits antiferromagnetic behavior, but unlike $Na_2BaMn(PO_4)_2$ vanadium compound do not indicate exotic phase transitions.
For the neutron experiment, we choose $Na_2BaMn(PO_4)_2$. This system exhibits antiferromagnetic behavior, strong frustration on the triangular lattice and the magnetic phase diagram contains possible exotic quantum phases (8), which makes this material quantum spin liquid candidate. Also, there are no neutron experiments performed on this material.

3 Sample Preparation

Inelastic neutron scattering described in section 1.5 is a very powerful experimental technique, but unfortunately suffers from low flux scattered from the sample. Traditionally, experimental physicists are coaligning big amounts of single crystals in order to have higher inelastic signal (32) when bigger crystals are not available. This is necessary also for $Na_2BaMn(PO_4)_2$ as its single crystals are tiny and in the form of thin plates with an average mass of 10 mg (see Fig. 4.1). To prepare $Na_2BaMn(PO_4)_2$ sample for inelastic neutron scattering, we developed the Automatic Laue Sample Aligner (ALSA).

3.1 Methods of crystal growth

In the early years of material research only natural minerals were studied, but with the development of the field, new methods for single crystal growth were necessary. In terms of crystal growth one of the first techniques usable on a large scale was flame fusion by Verneuil (33) (mainly used for ruby synthesis). In the first half of the twentieth century methods of crystal growth saw significant advances. Mainly new growth techniques of crystal growth were developed, hydrothermal growth, crystal pulling, the Bridgman method, and more. Nowadays the most notable crystal growth method is the Czochralski method, which is widely used not only by scientists but in industry as well. Czochralski method accounts for the most of the silicone production.

3.1.1 High-Temperature Solution Growth (Flux)

Multi-component compounds usually have high melting points or require other extreme conditions. Therefore it is difficult to grow such substances using conventional melting crystal growth methods. Crystallization of these compounds is carried out from a high-temperature solution where the temperature for their growth is much lower than their melting points. To crystallize the compound we first need to dissolve all components in a solvent at high temperature. Then, a supersaturation in the solution is attained by slow cooling of the solution or evaporation of the solvent such that crystals nucleate and grow in the supersaturated solution. Supersaturation can also be attained by creating a temperature difference between the locations of growing crystal and nutrient (34).
The main advantage of this method is that almost any material can be prepared. However, the solvent has to be chosen based on the knowledge of the composition of the material and has to be chemically similar. Based on this "comparability" of solvent and grown materials variety of impurities are introduced into grown crystals. The solvent should also have a low melting point, low vapor pressure, and low toxicity (35).
A typical growth experiment starts by weighing and mixing the required constituent material in the right ratio. The mixture is loaded into a crucible and is then placed into a furnace initially heated to the maximum temperature, then holding the crucible for several hours of soaking time to dissolve and homogenize the solution, slow cooling of the furnace to room temperature, and extracting grown crystals. The crystals obtained after growth can also be separated from the solution by decanting it (36).

3.2 Automatic Laue Sample Aligner (ALSA)

ALSA utilizes a robotic arm Meca500, Basler camera system, and conventional Laue X-ray diffractometer shown in figure 3.1.

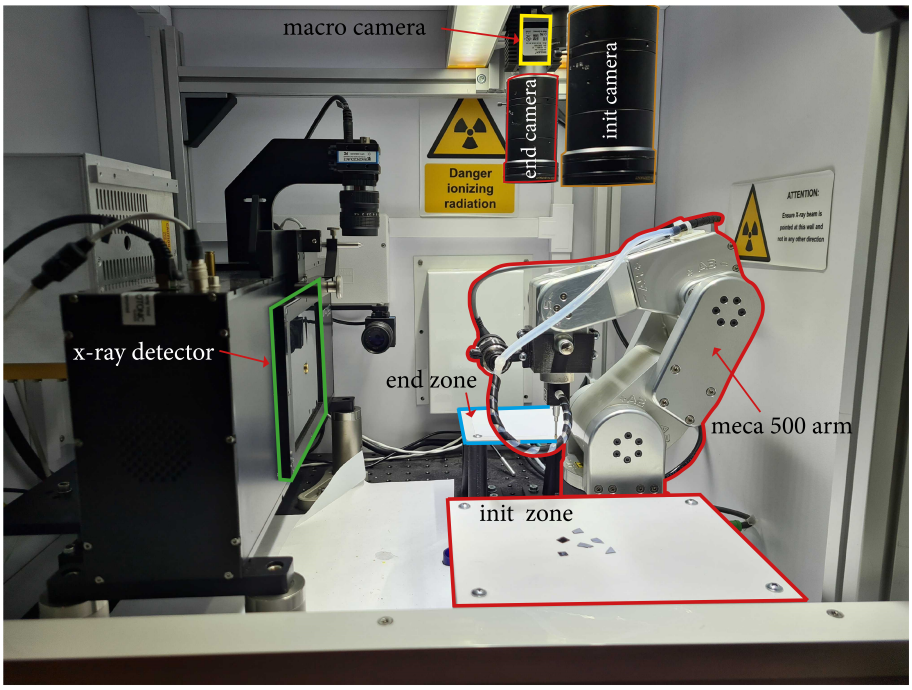

Figure 3.1: Inner space of ALSA containing 3 Basler cameras Laue X-ray diffractometer and robotic arm Meca500

The robotic arm in combination with PELCO Vacuum pic-up system, shown in figure 3.4, is able to automatically pick up crystals and move them between predefined zones. In each zone, a specific action is performed:

- **Init zone** - Crystals meant for coaligment are placed into this zone. The init camera takes a picture and detects crystals, as shown in figure 3.2, and saves the position of their center of mass. The robotic arm then picks up the crystal in the center of mass and moves it into X-ray zone.

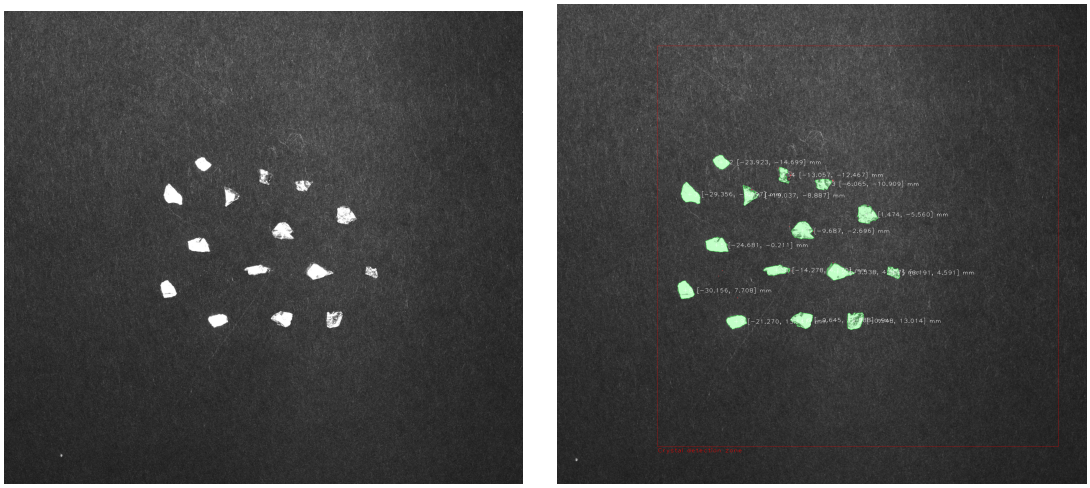

(a) Raw image (after camera calibration) form Init camera

(b) Detected crystals with calculated center of mass

Figure 3.2: Crystal detection in Init zone

- **Xray zone** - Crystal in this zone is placed in front of diffractometer and the Laue pattern is recorded, which is then automatically processed (this process is described in section 3.3) and crystal orientation is obtained. The robotic arm than moves the crystal in the correct orientation into the Macro zone.
- **Macro zone** - Crystal in correct crystallographic orientation is placed in front of the Macro camera and its exact shape is detected, as shown in figure 3.3.

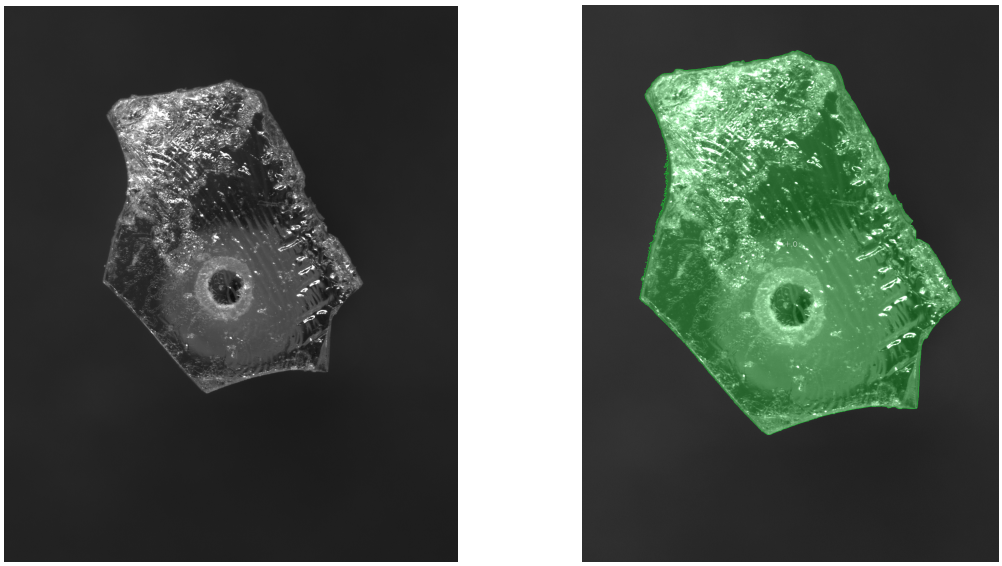

(a) Raw black and white image from Macro camera

(b) Detected borders of crystal, highlighted by green line

Figure 3.3: Crystal shape detection in Macro zone

- **End zone** - In the End zone we place a custom plate to place our crystal on. The position of this plate is detected by ArUco markers (37) glued to

a predefined position on the plate, shown in figure 3.4b. To calculate the optimal position of each crystal on the plate we use 2D irregular bin packing problem solution (38) (function is demonstrated in figure 3.5) implemented into our system. Before placing the crystal onto a plate, it is coated in glue. We use hydrogen-free glue CYTOP, which is based on amorphous fluoropolymer, completely without hydrogen making it perfect for neutron experiments (39).

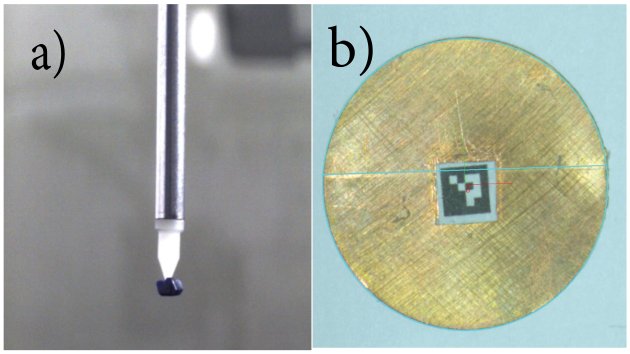

Figure 3.4: a) Tip of PELCO system holding a crystal. This tip is connected to the pump that creates negative pressure, holding the crystal in place. b) Copper plate with ArUco marker number 0. Through ArUco marker detection system located the plate and its shape.

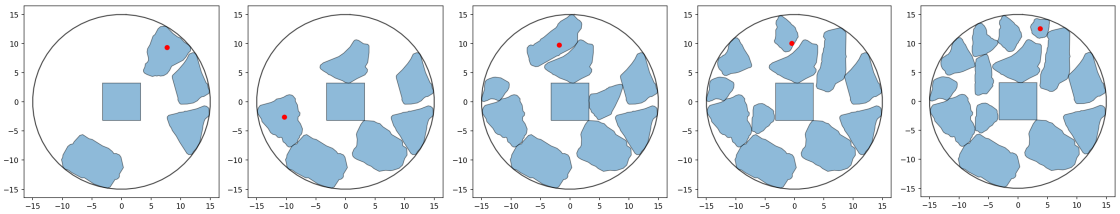

Figure 3.5: Additive process of adding crystal-shaped polygons. We choose 5 steps in the addition process (the red dot highlights the polygon that has been added last).

3.3 Coaligment algorithm

In section 3.2 we briefly introduced ALSAs parts and basic workflow and in this section we will focus on coaligment algorithm.
Basic overview of ALSA workflow is in figure 3.6.

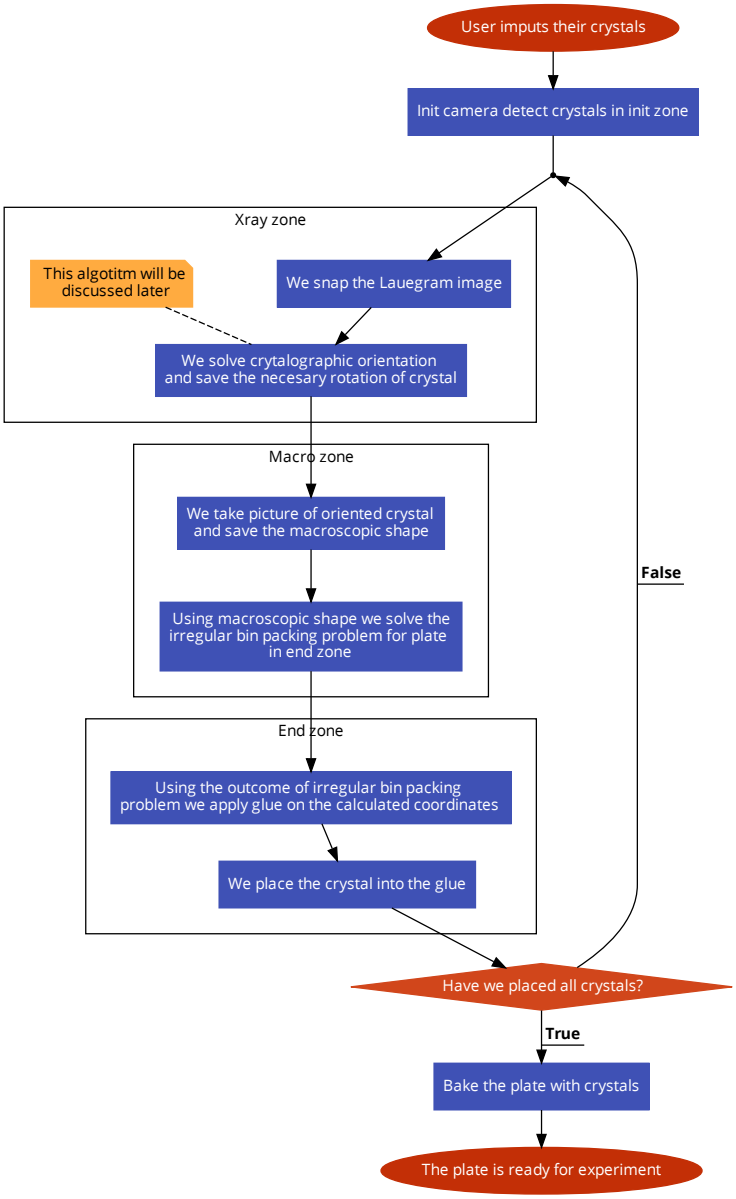

Figure 3.6: Workflow of ALSA in pseudo code. Code is divided into three sections based on robot zones.

The algorithm for solving the crystal structure relies on the known trigonal crystal structure of the crystals as described in section 2.1 and it is combined with the macroscopic shape of grown crystals. The main face of the crystal is perpendicular to the c axis, which creates six-fold symmetry in the Lauegram. The algorithm itself can be divided into consecutive parts:

- **Peak detection** - For implementation, we choose Python as a programming language. And for image processing, we use OpenCV2 library (40). Our function requires a certain intensity threshold, which determines the difference between peaks and background. The functionality of our code is demonstrated in figure 3.7.
- **Finding of the circle** - Coordinates of peaks in Lauegram (in pixels) are transferred into the detector coordinate system (in millimeters) using de-

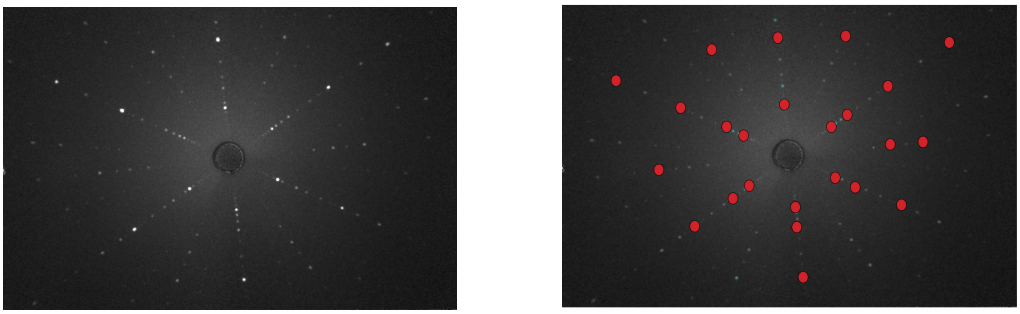

Figure 3.7: Raw lauegram, on the left, with acquisition time of 60 seconds and processed lauegram with detected peaks highlighted by blue contour

tector size. Then we loop through pairs of peaks creating circles (the center of the circle is between these two peaks and the diameter is the distance between these two peaks). There are two conditions for finding the right orientation. There have to be exactly six peaks on the circle and their mutual angle has to be sixty degrees. The algorithm returns the center of the circle and the position of those six peaks, demonstrated in figure 3.8.

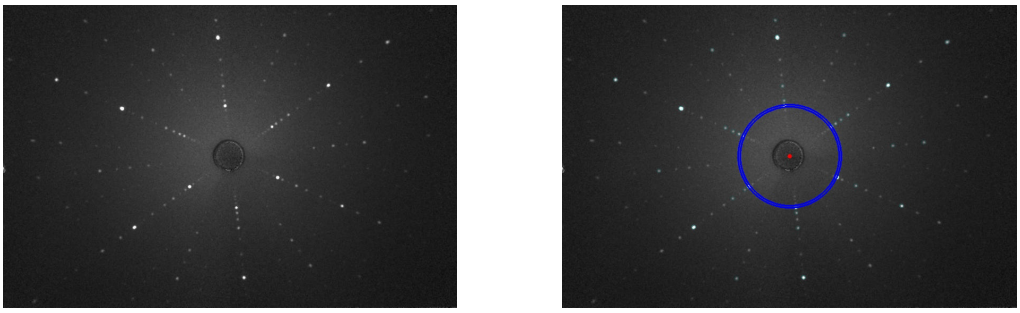

Figure 3.8: Raw lauegram, on the left, with acquisition time of 60 seconds and lauegram with determined circle and its center.

- **Determining macroscopic angles of rotation** - From the position of the center we can calculate rotations leading the crystal to align its c axis perpendicular to the detector. We basically imagine c axis as a vector and we want to rotate this vector using Euler angles. This task has a solution implemented into our algorithm.
  The alignment of a axis is calculated from the position of individual peaks. We want to align the a axis with x axis of the detector. We can calculate the angle between the peak and the x axis for each peak and then rotate the crystal around c axis to get to the orientated position. Due to the 6-fold symmetry, rotation by 60° also satisfies final condition.

4 Results and Discussion

4.1 Crystal growth

Single crystals for susceptibility, specific heat, magnetization and neutron experiments were synthesized by the flux method described in section 3.1.1. Dried Na_2CO_3, $BaCO_3$, MnO and $(NH_4)_2HPO_4$ were mixed stoichiometrically and grinded well with the flux media NaCl in a molar ratio of 1:5 (25). The mixture was loaded into an alumina crucible and then heated up to 950 °C for 2 h followed by a slow cooling to 750 °C. The obtained transparent single crystals were manually separated from the bulk. Typical dimension of the crystals is ∼1.5-4.0 mm in edge length and ∼0.3 mm in thickness. $Na_2BaMn(PO_4)_2$ single crystal are transparent in color, as shown in figure 4.1, and are planar in shape with planes perpendicular to the c axis.

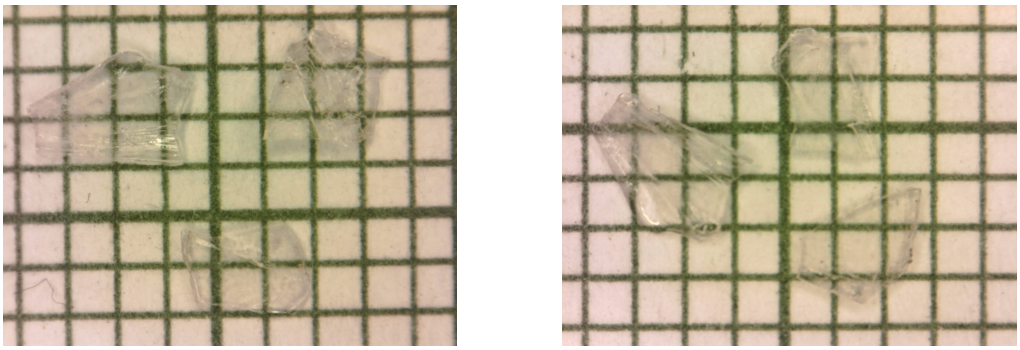

Figure 4.1: Photograph of multiple single crystals varying in size on 1×1 mm^2 grid.

We used the ALSA machine to check the quality of our crystals. The Lauegrams of the [001] plane are shown in figure 4.2. In this figure the (110) and (100) directions are highlighted. The two crystallographic directions are important for the neutron experiment in section 4.3. This crystal orientation will enable us to scan in (110)×(001) plane.

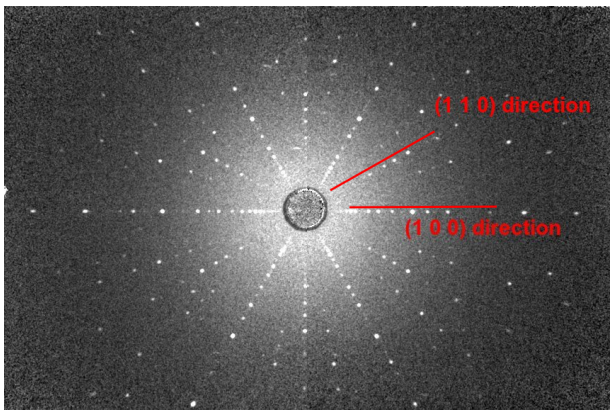

Figure 4.2: Lauegram with an acquisition time of 60 seconds with highlighted (110) and (001) directions.

To probe the inner structure of grown crystals we measured powder diffraction on Bruker D8 Diffractometer in the Bragg-Brentano geometry. Measured spectrum is in figure 4.3 and was collected at room temperature. The profile refinement was done by Rietveld refinement using FullProf suite. The best fit was achieved with the space group P$\bar{3}$m1 and lattice parameters $a = b = 5.3791(1)$ $\AA$ and $c = 7.1041(2)$ $\AA$. The Crystallographic coordinates were extracted and are in table 2.

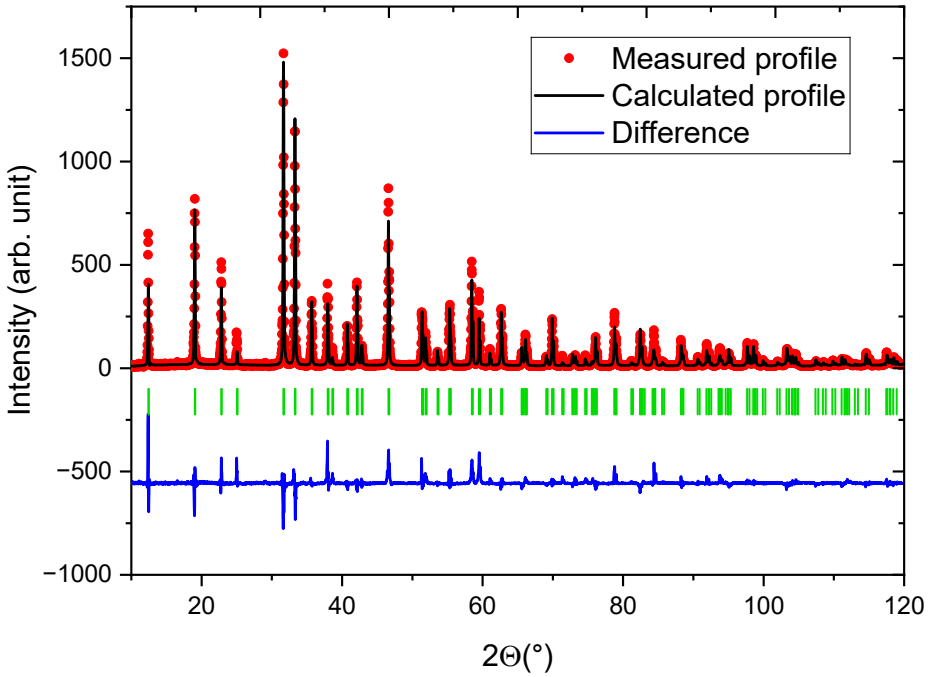

Figure 4.3: Rietveld refinement of $Na_2BaMn(PO_4)_2$ at room temperature using FullProf Suite with Bragg R-factor 14.07. Green lines denote peaks expected from symetry P$\bar{3}$m1.

Atom	Wyckoff	x	y	z	Occupancy
Na	2d	2/3	1/3	0.773(2)	0.15(8)
Ba	1b	0	0	1/2	0.071(4)
Mn	1a	0	0	0	0.064(4)
P	2d	2/3	1/3	0.191(1)	0.09(6)
O_1	2d	2/3	1/3	0.444(1)	0.2(1)
O_2	6i	0.1686(8)	0.8314(8)	0.8096(8)	0.4(2)

Table 2: Crystallographic coordinates extracted from the Rietveld refinement carried out using X-ray powder diffraction data at room temperature

Refinement of this structure proved to be very complicated due to large preferential orientation in direction (001). This large preferential orientation comes

from the plate-like shape of crystals with c axis perpendicular to the plate. Occupancy in table 2 are normalized so they add up to one. The chemical content of the unit cell is $Na_{2.2(2)}Ba_1Mn_{0.9(1)}P_{1.4(8)}O_{8.8(9)}$. Due to a large error that exceeded 60% for some atoms the quantitative analysis or our sample is not reliable. However, all of the observed peaks are indexed, which means that our crystals do not contain another phase.

4.2 Bulk measurements

To probe the magnetic properties of this material we measured the temperature dependence of DC susceptibility and magnetic field dependence of magnetization by Quantum Design Vibrating Sample Magnetometer (VSM) for the Physical Property Measurement System (PPMS) and temperature dependence of specific heat was measured by Quantum Design Heat Capacity System for the PPMS.

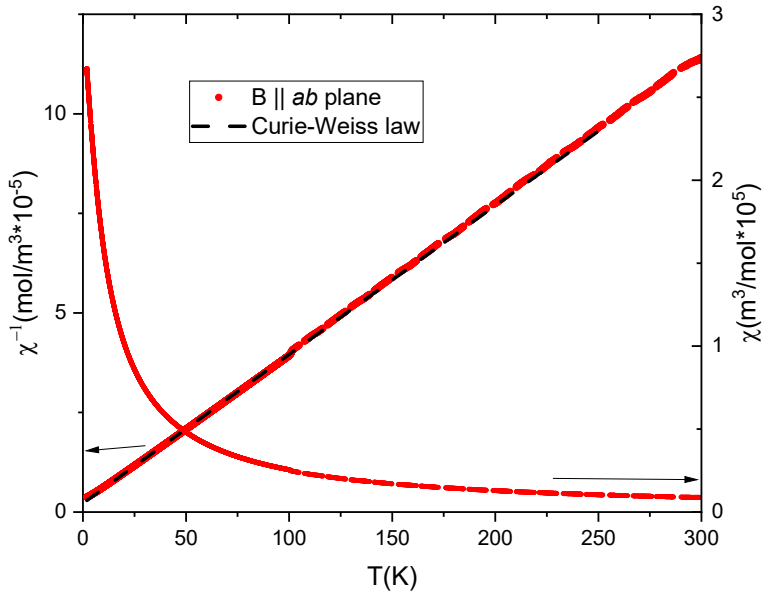

Figure 4.4: Temperature dependence of magnetic susceptibility measured in ab plane in the magnetic field 0.1 T.

Temperature dependence of DC susceptibility was measured in magnetic fields of 0.1 T, 1 T, 10 T, and 14 T in temperature range 2 - 300 K. In this range the χ(T) curve shows a monotonic increase with temperature without any signature of long-range order. Susceptibility in a magnetic field was measured in two crystallographic directions along c axis and in ab plane except in the magnetic field 0.1T where susceptibility was measured only in ab plane as shown in figure 4.4. We applied Currie-Weiss model at 50 K $\leqq$ T $\leqq$ 250 K and found that the CW temperature Θ_{CW} = -5.88(1) T and effective magnetic moment of Mn^{2+} μ_{eff} = 6.5(9) μ_B. This value of the effective magnetic moment is larger than expected for spin-only Mn^{2+} calculated from equation 1.14 as 5.92 μ_B. The frustration ratio

defined in equation 1.18 for this material $f_1 = 5.9(3)$, where the index of frustration ratio corresponds to phase transition in the ground state in figure 4.11. This value of frustration ratio is similar to other $2d$ triangular lattice Heisenberg antiferromagnetic systems such as $Rb_4Mn(MoO_4)_3$ (7.14) (41), $RbFe(MoO_4)_2$ (5.79) (42) and $Na_2BaNi(PO_4)_2$ (4.3) (26).

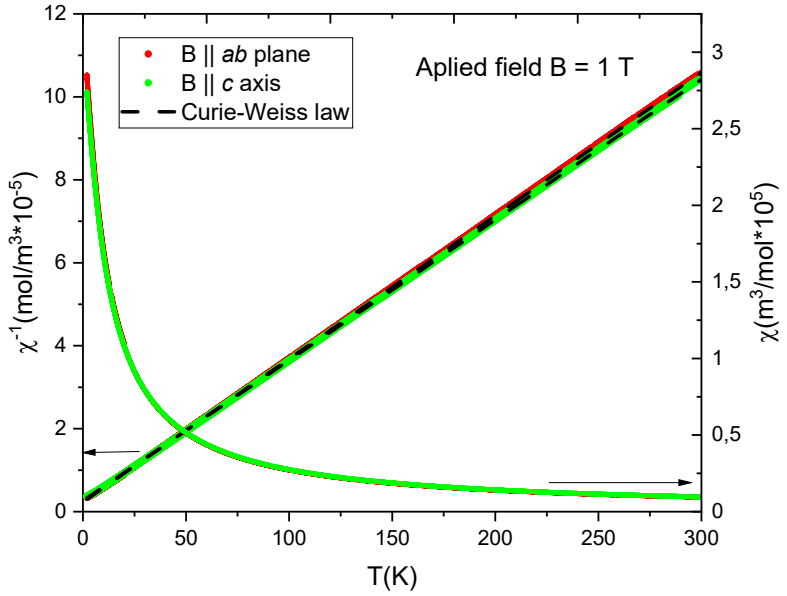

Figure 4.5: Temperature dependence of susceptibility measured along two crystallographic directions from 2K to 300 K in magnetic field 1 T.

The magnetic susceptibility was measured in higher magnetic fields 1 T in figure 4.5, 10 T in figure 4.6 and 14 T in figure 4.7 along c axis and in ab plane. The susceptibility was also fitted by Curie-Weiss law and the results are summarized in table 3. The anisotropy ratio ($\equiv \chi_{\parallel c}/\chi_{\parallel ab}$) at minimal measured temperature 2 K is 0.96(1) for 1 T, 1.01(3) for 10 T and 1.03(2) for 14 T.

		$\parallel c$	$\parallel ab$
B = 1 T	Θ_{CW} (K)	- 7.75(1)	- 6.74(1)
	μ_{eff} (μ_B)	6.8(2)	6.9(2)
B = 10 T	Θ_{CW} (K)	- 8.88(3)	- 16.43(5)
	μ_{eff} (μ_B)	7.1(6)	7.7(8)
B = 14 T	Θ_{CW} (K)	-12.94(4)	-21.67(6)
	μ_{eff} (μ_B)	7(2)	7(2)

Table 3: Result of Curie-Weiss fit of susceptibility in different magnetic field.

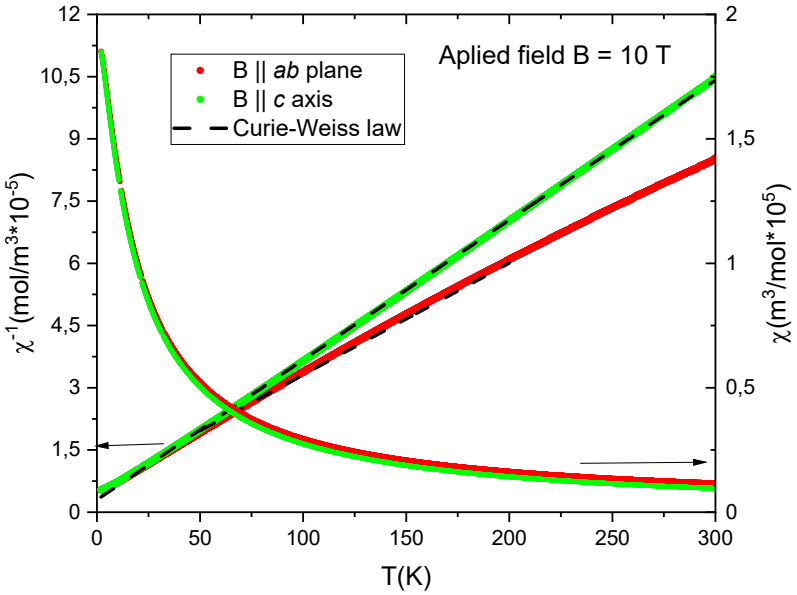

Figure 4.6: Temperature dependence of susceptibility measured along two crystallographic directions from 2K to 300 K in magnetic field 10 T.

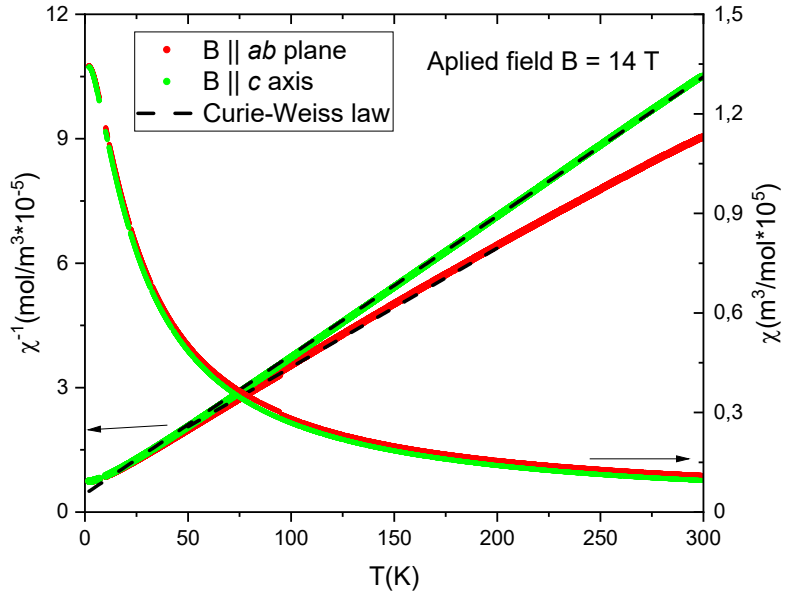

Figure 4.7: Temperature dependence of susceptibility measured along two crystallographic directions from 2K to 300 K in magnetic field 14 T.

Magnetization measurements at 2 K along c axis and in ab plane in the magnetic field range from 0 to 14 T is in figure 4.8. Magnetization at this temperature shows isotropic behavior for both directions. The slope starts to saturate at 6 T and fully saturates around 12 T at a value 4.9(1) μ_B/Mn. The theoretical

saturated magnetization is $gS\mu_B$ and is equal to 5 μ_B/Mn if only considering the spin moment, which is consistent with the observed value.
Magnetization was also measured at higher temperatures of 5 K, 10 K and 15 K in *ab* plane in figure 4.9 and at temperatures 5 K, 10 K, 15 K and 50 K along *c* axis in figure 4.10. At higher temperatures, magnetization does not saturate up to the maximum measured magnetic field. The magnetization anisotropy ratio stays close to one for all measured temperatures. In higher temperatures, the dependency is not linear but does not saturate up to the maximum magnetic field measured.

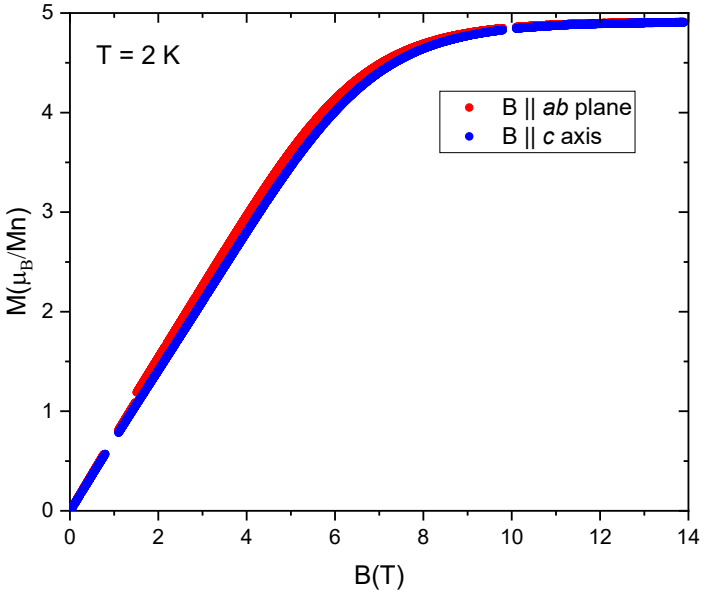

Figure 4.8: Magnetic field dependency of magnetization at 2 K measured along *c* axis and in *ab* plane.

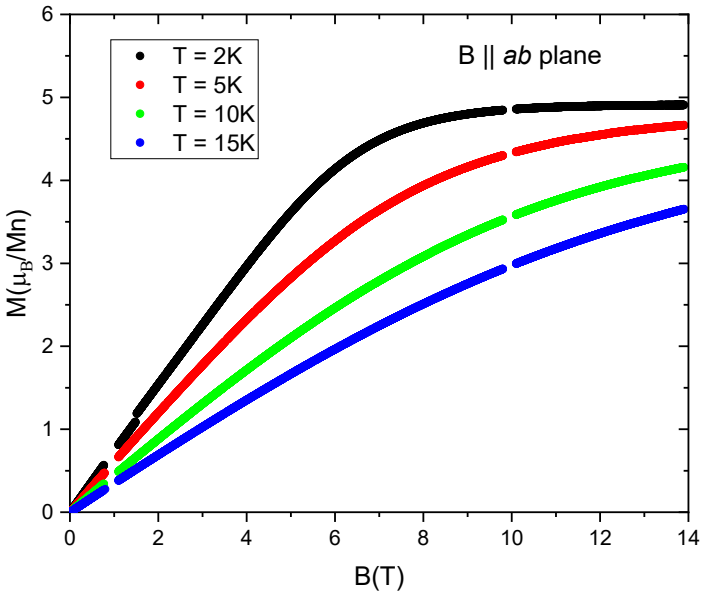

Figure 4.9: Magnetic field dependency of magnetization at temperature 2 K, 5K, 10 K, and 15 K in *ab* plane.

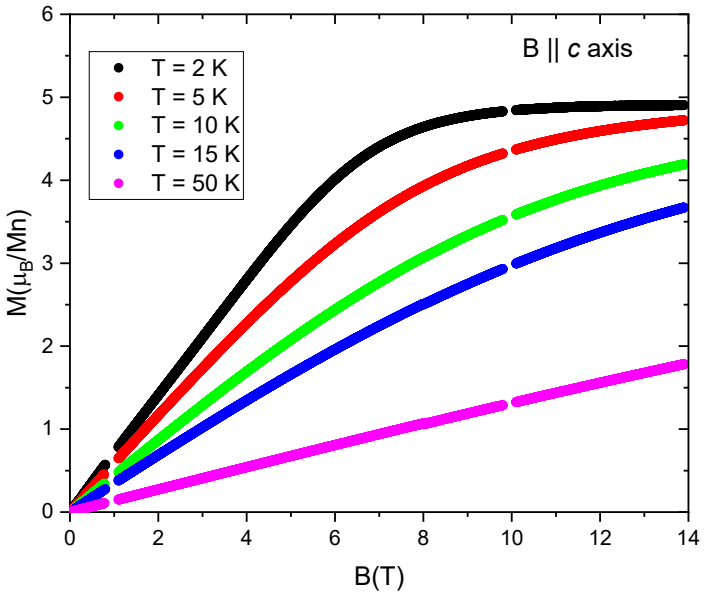

Figure 4.10: Magnetic field dependency of magnetization at temperature 2 K, 5K, 10 K, 15 K, and 50 K along *c* axis.

To further study the phase transition at lower temperatures, we measured the specific heat down to 0.5 K. Figure 4.11 shows the C_P(T) curve under 2 K without applying a magnetic field. The peak features at low temperatures indicate magnetic long-range order and two-phase transitions. From the maxima of two

peaks, we determined Néele temperature as $T_{N1} = 1.1$ K and $T_{N2} = 1.3$ K.

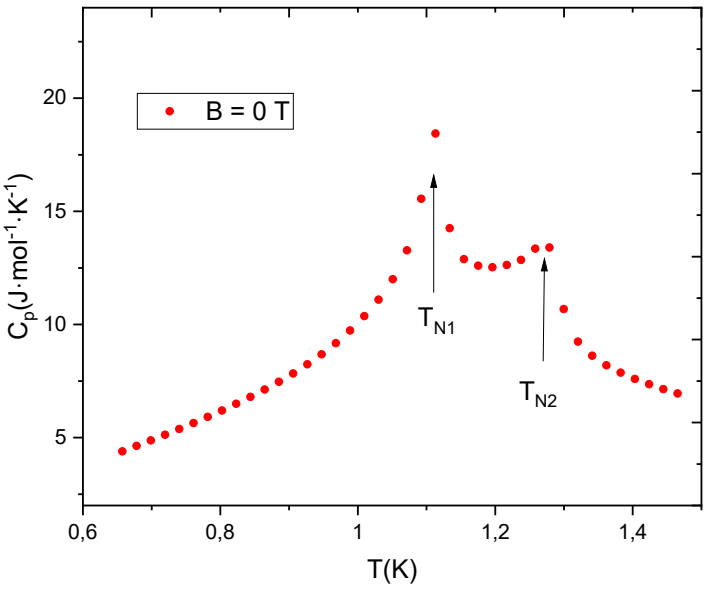

Figure 4.11: Specific heat measured below 2 K in zero magnetic field revealing Néele temperature for this system.

To map out the magnetic phase diagram we measured the temperature dependence of specific heat from zero magnetic field up to 9 T with step 0.1 T. Constructed contour phase diagram with applied magnetic field along c axis is in figure 4.12. Since we measured temperature dependence of specific heat it is hard to properly distinguish individual phases that have a constant boundary in temperature. To properly see the development of those phases we constructed field dependency of specific heat shown in figure 4.13 as an artificial cut from the dataset. Red lines in figure 4.12 represent scans in figure 4.13 and red stars in figure 4.12 represent phase transitions denoted as black stars in figure 4.13. At higher temperatures, we observed a very strong transition from fully polarized state to a magnetically ordered state at magnetic field ≈ 2.6 T. This boundary shifts to higher fields with lower temperatures and around 0.9 K splits into two phases and at temperature 0.9 K one of the phase transitions disappears and one splits into two. The boundary between the fully polarized state and the magnetically ordered state stays visible down to the minimal temperature measured, but phase transition visible at 0.8 K and around 4 T disappears at temperature 0.6 K.
At lower temperatures, there is also another phase transition. This phase transition originates from the peak at 1.1 K in zero field which moves to 0.8 T at 1 K and then slowly rises in magnetic field with decreasing temperature.

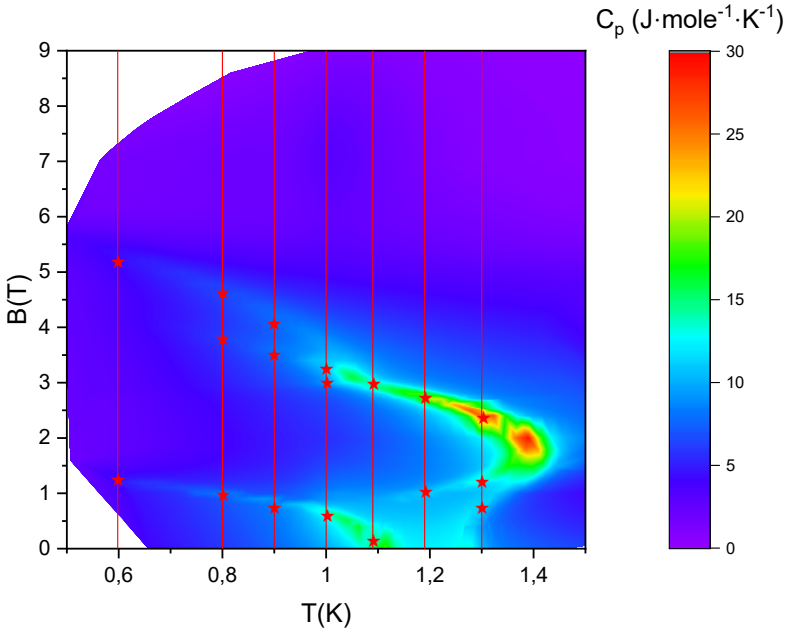

Figure 4.12: Map of specific heat constructed from temperature scans with different applied fields with step 0.1 T. Red lines correspond to field scans and red stars correspond to black stars in figure 4.13.

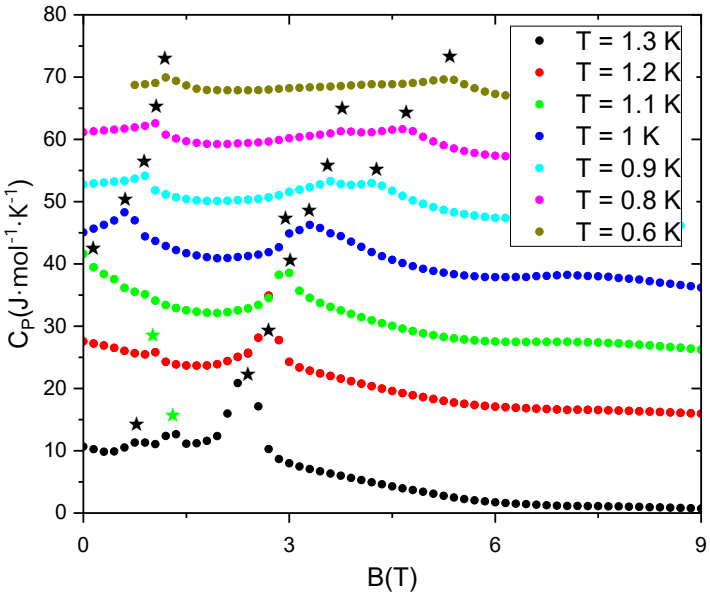

Figure 4.13: Magnetic field dependant specific heat at different temperatures. All curves except for T = 1.3 K are sequentially shifted by 15 J·mol^{-1}·K^{-1} for clarity. Black stars denote the phase transition.

There is also a phase boundary at lower fields ≈ 0.6 T which is almost constant with lower temperatures. There is also a very weak phase transition at

magnetic field 1 T and temperature 1.2 K, which is in figure 4.13 denoted by green stars. This phase transition has not been reported (8) in the original phase diagram in section 2.1.3. To further probe this pocked phase we constructed field dependency of specific heat shown for temperatures 1.05 K, 1.1 K, 1.2 K, and 1.25 K shown in figure 4.14. The weak phase transition is denoted by black stars in figure 4.14. This pocket phase resembles the newly reported Vortex crystal phase (43), which has been reported for square lattice frustrated ferromagnet. The phase diagram of a square lattice frustrated ferromagnet with new phase Vortex crystal is in figure 4.15.

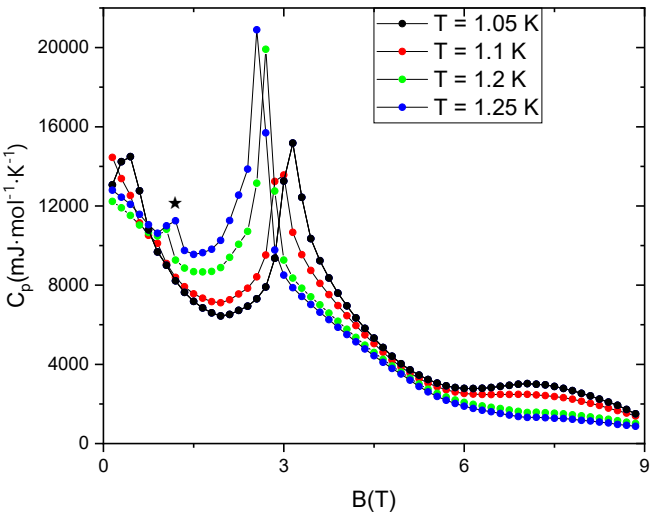

Figure 4.14: Magnetic field dependant specific heat around weak phase transition at ≈ 1 T. Black star denotes the weak phase transition of pocket phase.

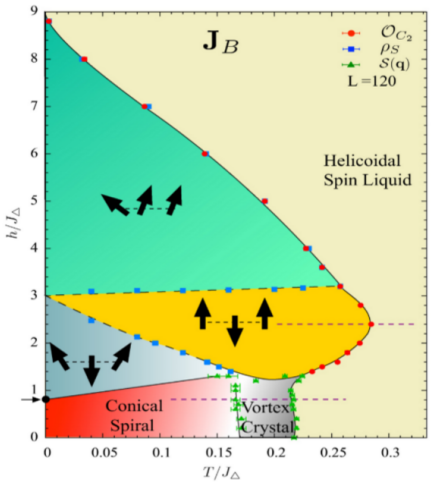

Figure 4.15: Finite size phase diagram of a square lattice frustrated ferromagnet in the applied magnetic field, showing classical spin liquid and at low fields vortex crystal (43).

We also probed the magnetic phase diagram with a magnetic field applied in *ab* plane with temperature scans of heat capacity in different magnetic fields from 0 T to 7 T with step 0.1 T shown in Figure 4.16. To properly see individual transitions we also constructed magnetic field scans in different temperatures in figure 4.18 and temperature scans of specific heat in different magnetic fields in figure 4.17. In these scans, we determined the positions of individual peaks corresponding to individual phase transitions. The peak at 1.1 K in zero magnetic fields up to the magnetic field of 0.9 T. Around magnetic field 1 T the phase boundary became constant in temperature and disappears under temperature 0.9 K. This is most likely a consequence of measuring only temperature dependency of specific heat, where this phase transition is hidden between individual scans.

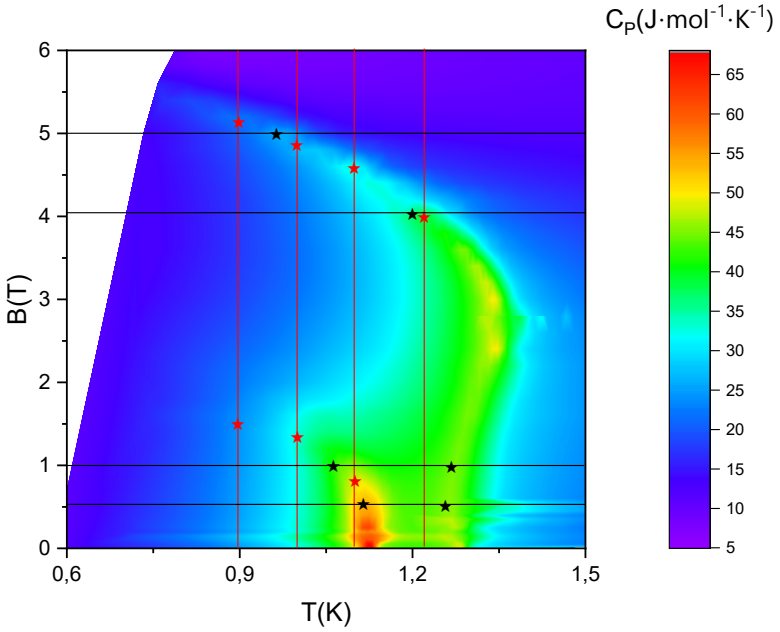

Figure 4.16: Map of specific heat constructed from temperature scans with different applied magnetic fields in *ab* plane with step 0.1 T. Red lines and red stars corresponds to scans and peaks in figure 4.18 and black lines and black stars corresponds to scans and peaks in figure 4.17.

The second peak at temperature 1.3 K at zero fields indicates the phase boundary between the spin-polarized state and magnetically ordered state. The phase boundary stays at a temperature of 1.3 K up to a magnetic field of 3.5 T, where it starts to move to lower temperatures with an increasing magnetic field. This phase transition is clearly visible down to the minimal temperature measured.

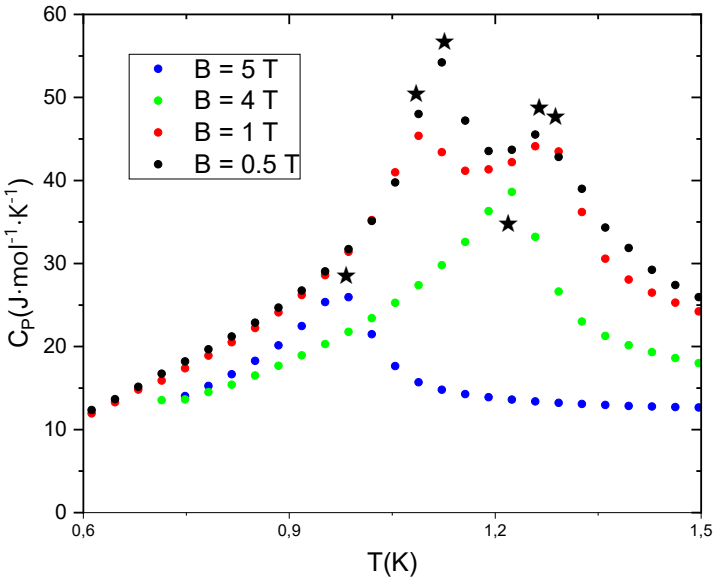

Figure 4.17: Temperature dependency of specific heat in different magnetic fields. Black stars denote the phase transition.

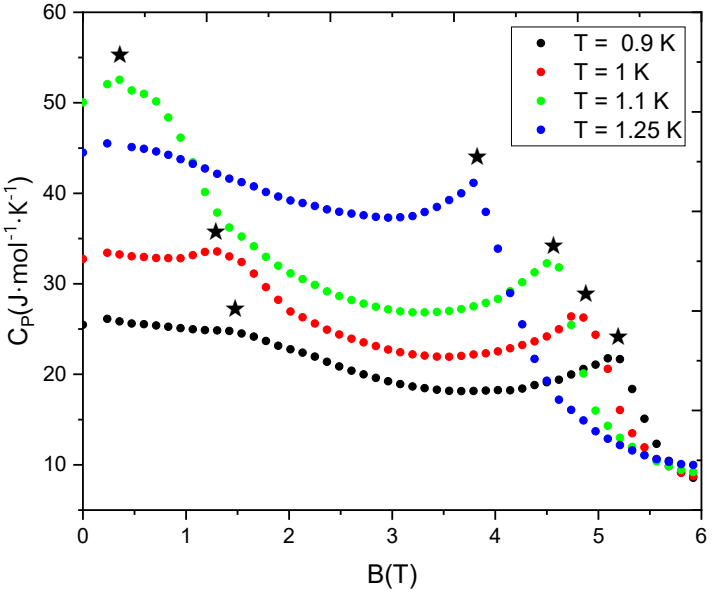

Figure 4.18: Magnetic field dependant specific heat at different temperatures. Black stars denote the phase transitions.

Our constructed phase diagrams were compared to the published phase diagrams (8) in figure 4.19 along c axis and in figure 4.20 in ab plane. Our phase diagrams correspond to the reported phase diagrams in general, however, we updated the phase diagram along the c axis by pocket phase determined as a

possible Vortex crystal phase (43).

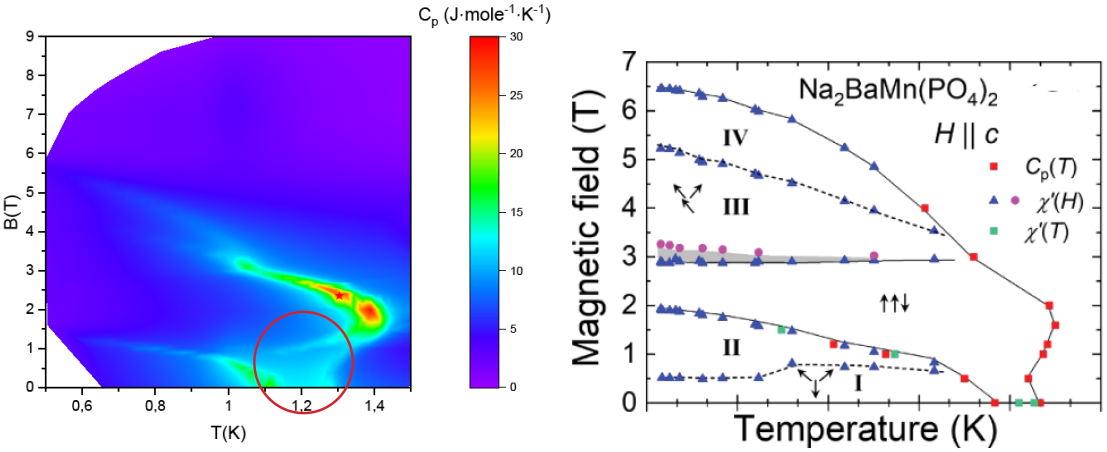

Figure 4.19: Comparison of our magnetic phase diagram on the left and published magnetic phase diagram (8) on the right with magnetic field applied along *c* axis. New Vortex crystal phase is highlighted by red circle.

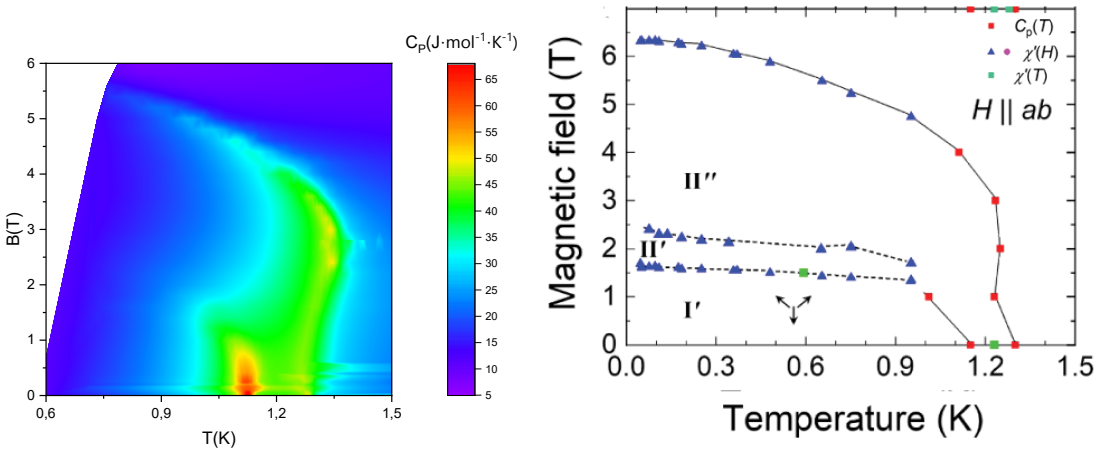

Figure 4.20: Comparison of our magnetic phase diagram on the left and published magnetic phase diagram (8) on the right with magnetic field applied in *ab* plane.

4.3 Neutron experiment

Neutron experiments were carried out at Institute of Laue-Langevin (ILL) at cold neutron triple-axis spectrometer IN12 (Instrument is described in appendix B). This master thesis contains two experimental measurements on IN12 with proposal number 4-01-1795 (44) and CRG-3066 (45). In addition our scientific team performed measurements on thermal neutron two-axis diffractometer D23 with proposal numbers 5-41-1252 and CRG-3064. These two experiments on D23 will be referenced in this thesis, but only to support data from IN12 or other measurements.

4.3.1 Coaligment results

Using ALSA described in section 3.2 two samples were prepared (see figure 4.21). The first sample (see figure 4.21a) was used in the experiment on IN12 with proposal number 4-01-1795. Sample consisted of six copper plates connected by a middle piece ensuring the plates are parallel. Crystals on each plate were coaligned to have the same crystallographic directions. Plates were coaligned together using instrument OrientExpress (46).

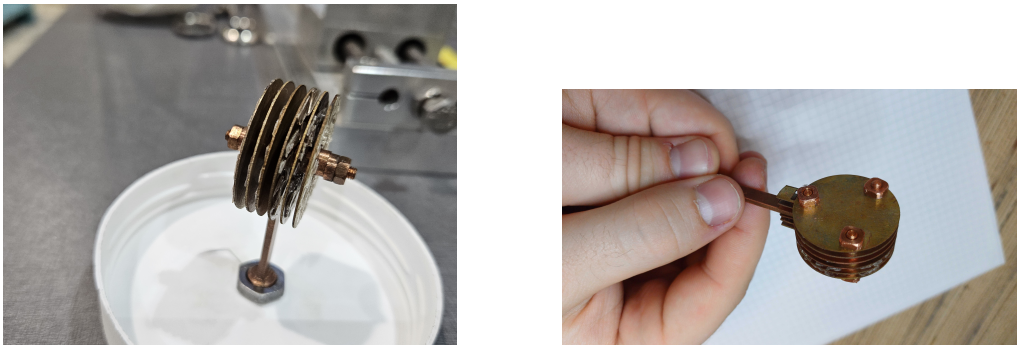

(a) (b)

Figure 4.21: a) The original sample of over 200 coaligned crystals with a mass over 2 g. b) Improved sample of 300 coaligned crystals and mass over 3g

To measure the overall mosaicity using the IN12 we scanned at temperature 5 K the angular dependence of nuclear Bragg peaks (002) (see figure 4.23) and (110) (see figure 4.23) to see the mosaic spread of c axis and ab plane.
The result of crystal coaligment done by ALSA is summed up in the table 4, 84% of crystal mass with FWHM of 4.06° has ab plane oriented in the same direction. The disarrangement of crystals ab plane is caused by the growth of crystals and how are the crystals placed on the copper plate.This disarrangement is impossible to get rid of, because of the non perfect surface of the crystals. The satellite peaks around the main one consisting of 15% of crystal mass indicates that some crystals are lying on top of each other or are grown imperfectly.
The crystal c axis misalignment forms four peaks which are described in table 5. It is clear that peak3 and peak4 have almost double the intensity of peak1 and peak2. If we compare those intensity ratios with the individual weight of crystals on each plate, we can see that peak1 and peak2 correspond to plate with crystal mass 0.31 g and 0.35 g and peak3 and peak4 correspond to plates with crystal mass (0.38 + 0.33) g and (0.33 + 0.32) g. This split is caused by the misalignment of individual plates. The width of individual peaks is below 2.2°.

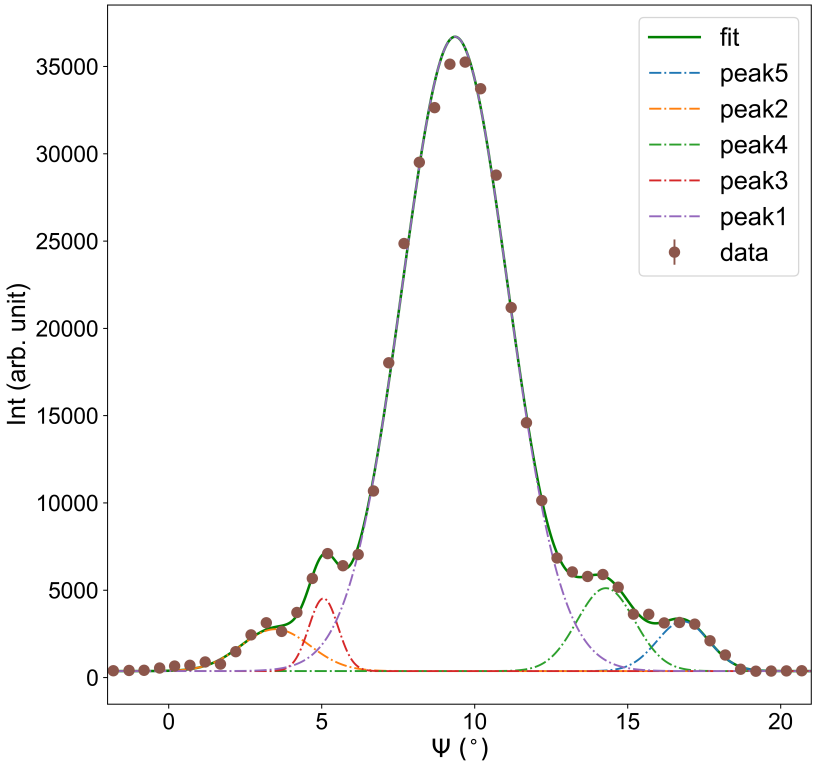

Figure 4.22: The mosaic spread of the older sample in *ab* plane.

ab plane missorientation		
	Intensity ratio (%)	FWHM (°)
peak1	84	(4.06±0.02)
peak2	4	(2.2±0.2)
peak3	3	(1.1±0.1)
peak4	6	(2.2±0.2)
peak5	3	(2.0±0.1)

Table 4: Missorientation of *ab* plane of all crystals

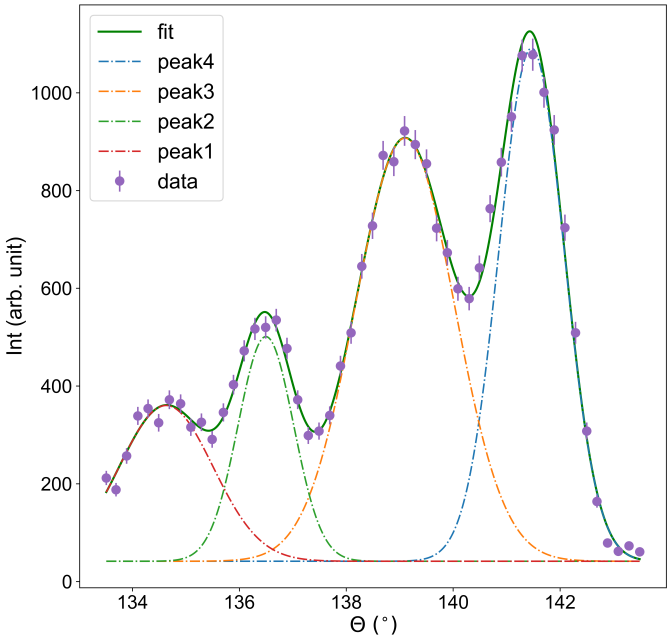

Figure 4.23: The mosaic spread of the older sample in c axis.

c axis missorientation			
	Intensity ratio (%)	FWHM (°)	Crystal weight (g)
peak1	15	(2.1±0.2)	0.31
peak2	12	(1.22±0.09)	0.35
peak3	40	(2.18±0.08)	0.38 + 0.33
peak4	33	(1.43±0.04)	0.33 + 0.32

Table 5: Missorientation of c axis of all crystals

To negate the misalignment of individual plates we added two supporting copper rods to hold individual plates in the same mutual orientation (see figure 4.21b). To check the overall misalignment we preformed angular scan at temperature 300 K of Bragg peaks (002) for c axis (see figure 4.25) (-1-10) for ab plane (see figure 4.24) and (-1-1-1) for combined c axis and ab plane (see figure 4.26). For this newer sample, the result of the coalignment is in the table 6. The misorientation of ab plane looks better as 72 % of crystal mass with FWHM of 1.9°. This result is caused bz better quality of single crystals grown in next batch.
The c axis misalignment of this new sample is summarized in table 7. The problem of misaligned plates seems to be solved with this new technique since 92 % of crystal mass with FWHM 2.93° shares the same direction. There are additional satellite peaks, but their combined intensity is below 10 %, these are caused by mistakes in crystal placing an will be improved in the future. However, this result seems to be sufficient for the inelastic neutron experiment. ALSA should be able to perform better coalignment with FWHM below 2° as we observed in the first sample.

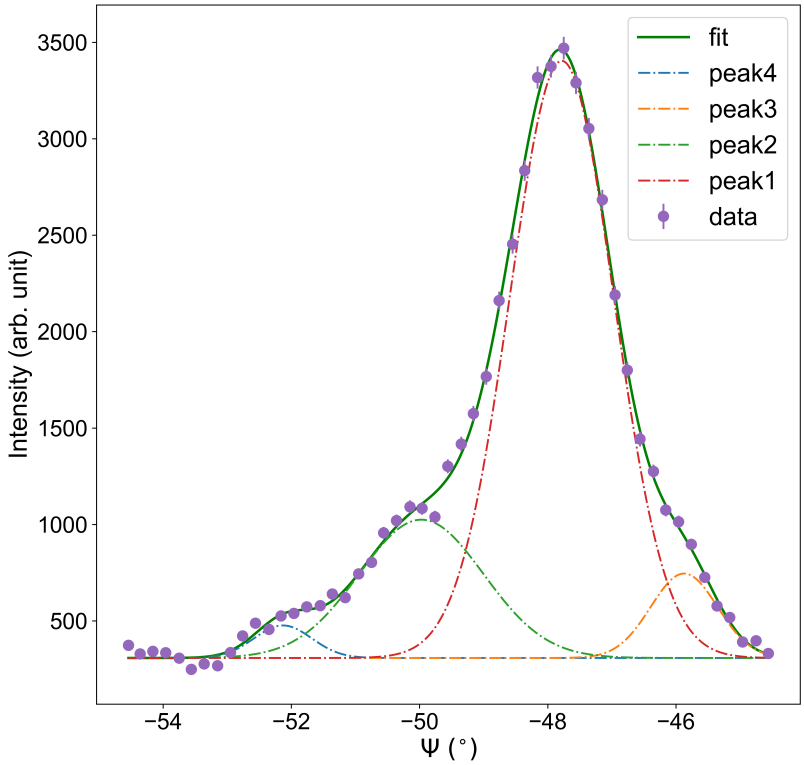

Figure 4.24: The mosaic spread of the new sample in *ab* plane.

ab plane missorientation		
	Intensity ratio (%)	FWHM (°)
peak1	72	(1.9±0.1)
peak2	20	(2.3±0.5)
peak3	6	(1.2±0.2)
peak4	2	(1.1±0.3)

Table 6: Missorientation of *ab* plane of all crystals on the new sample

c axis missorientation		
	Intensity ratio (%)	FWHM (°)
peak1	92	(2.93±0.05)
peak2	6	(0.91±0.01)
peak3	2	(1.1±0.3)

Table 7: Missorientation of *c* axis of all crystals on the new sample

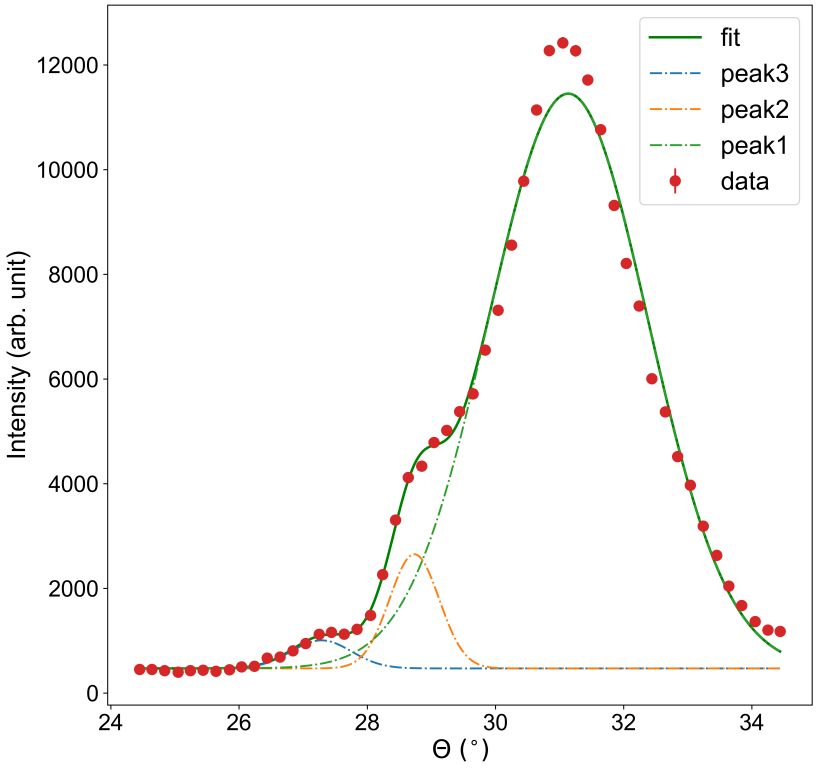

Figure 4.25: The mosaic spread of the new sample in c axis.

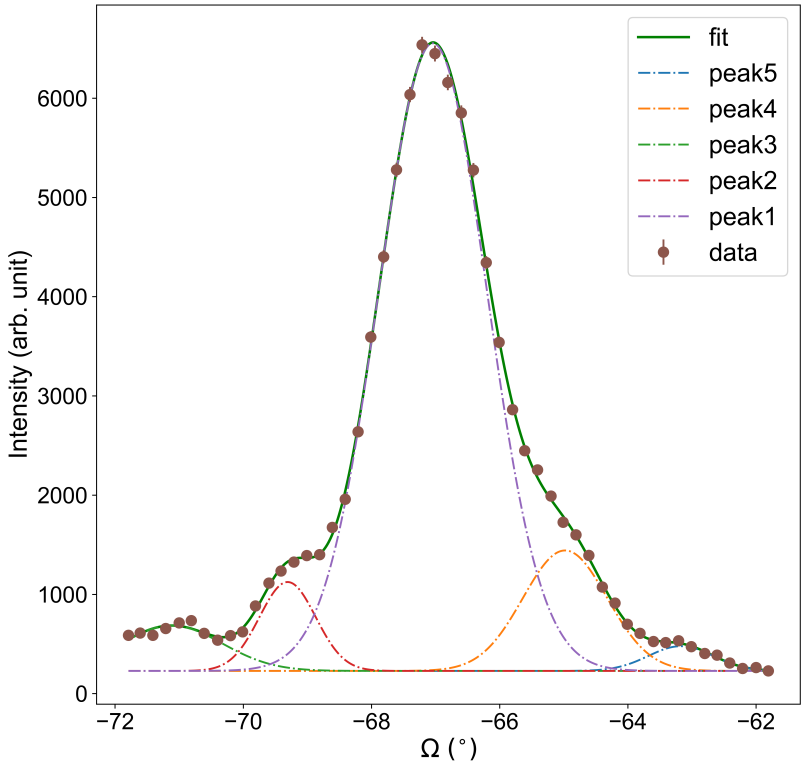

Figure 4.26: The mosaic spread of combined c axis and ab plane

combined misorientation of c axis and ab plane		
	Intensity ratio (%)	FWHM (°)
peak1	76	(1.98±0.01)
peak2	6	(1.03±0.07)
peak3	5	(1.8±0.2)
peak4	11	(1.5±0.1)
peak5	2	(1.2±0.2)

Table 8: Combined misorientation of c axis and ab plane

The result of the combined misarrangement of crystals is summarized in the table 8. The sample is definitely suitable for an inelastic neutron experiment with 76 % of crystal mass with FWHM 1.98° correctly coaligned. This result of ALSA is very promising but can be improved to over 95 % mass of aligned crystals through hardware and software improvements.

4.3.2 Determination of propagation vector

From the single crystal neutron diffraction experiment on IN12 (44) we discovered magnetic peaks at temperature 60 mK (see figure 4.27) suggesting long-range magnetic order. To determine if this peak is magnetic we measured the temperature dependence of this peak shown in figure 4.28. Magnetic Bragg peak

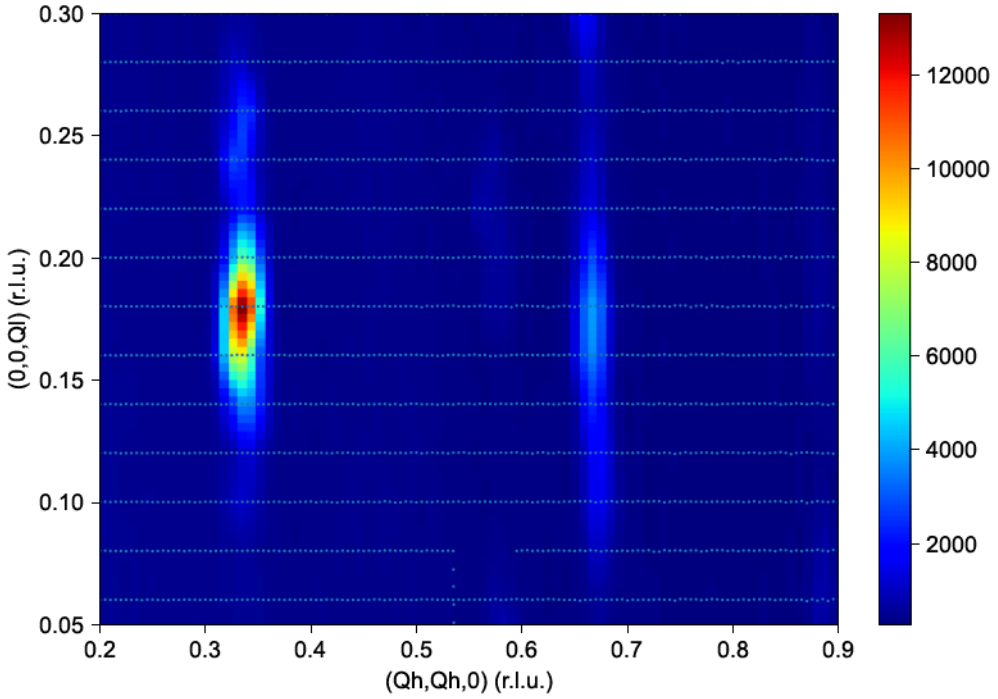

Figure 4.27: (Qh,Qh,Ql) scattering plane measured at 60 mK below Neéle temperature in zero field with Qh scans and Ql step 0.02.

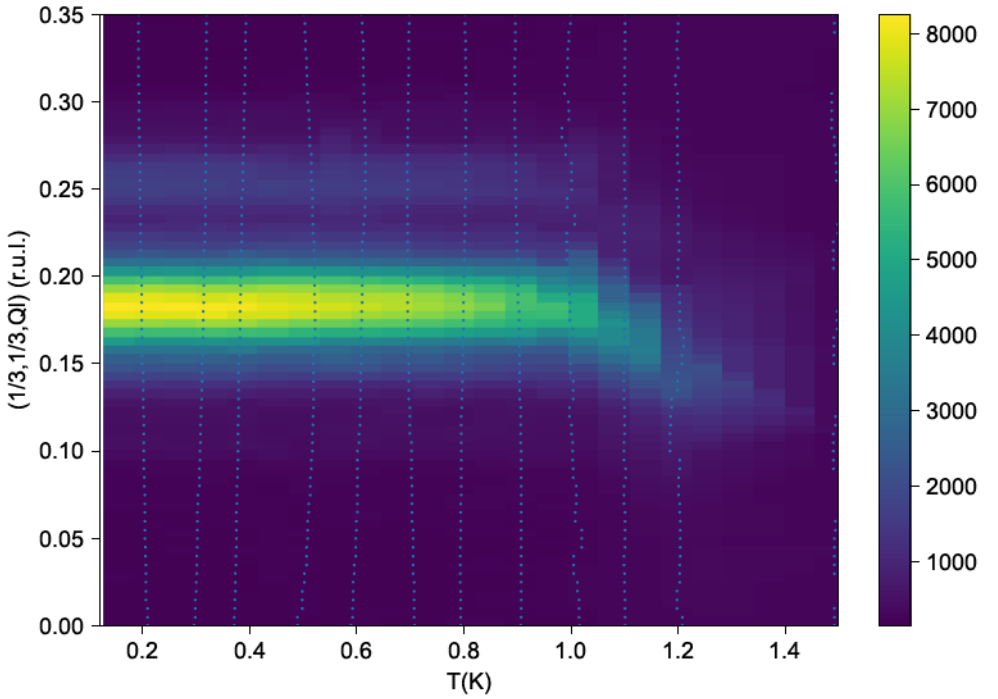

Figure 4.28: Temperature dependence of the position of the magnetic Bragg peak.

disappears above the temperature 1.2 K which is consistent with the magnetic phase diagram and it proves that observed peaks are of magnetic origin.
Our sample was prepared so that we are scanning in [hh0]×[00l] planes, which means we can do scans in (Qh, Qh, 0), (0, 0 ,Ql) and directions combining the previous two directions. We observe two magnetic peaks corresponding to the propagation vector of the ground state. To properly determine the propagation vector both peaks were fitted by 2D Gaussian function. The brighter peak shown in figure 4.29 has fitted maximum at Qh=0.3325(1) and Ql=0.176(2) with the FWHM along Qh 0.013(1) and along Ql 0.022(2) and the parasitic peak has maximum at Qh=0.331(5) and Ql=0.2498(9) with the FWHM along Qh 0.011(5) and along Ql 0.017(1). The parasitic peak has one-fifth of the main peak intensity. A less intense peak has fitted maximum at Qh=0.667(3) and Ql=0.179(1) with the FWHM along Qh 0.011(3) and along Ql 0.0414(1).

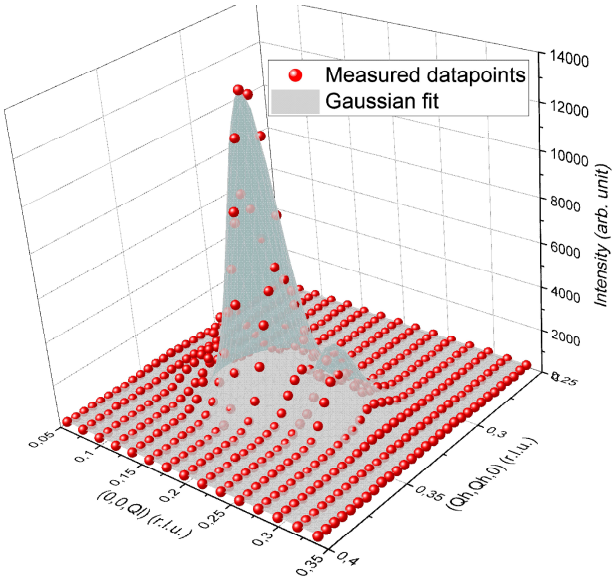

Figure 4.29: Magnetic Bragg peak with greater intensity with smaller parasitic peak fitted by 2D Gaussian function.

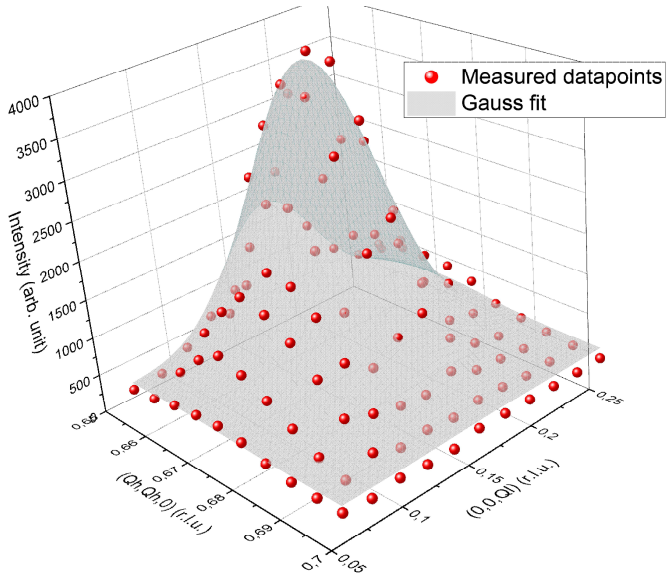

Figure 4.30: Less intense magnetic Bragg peak fitted by 2D Gaussian function.

Fitting magnetic Bragg peaks by 2D Gaussian is not very accurate because we have to account for the step in Ql direction. That means that the error is half the step so 0.01. Also from figure 4.27 we can see that the maximum intensity of the brighter peak is measured by Qh scan at Ql=0.18. This one-dimensional scan is shown in figure 4.31. In this scan, we fitted both peaks by the Gaussian function and we obtained a maximum of the brighter peak at Qh = 0.3330(7) with FWHM of 0.0284(4) and the maxim of the second peak at Qh = 0.6671(2) with FWHM of 0.02402(5). From the discussion above we conclude that the propagation vector in the ground state is (1/3,1/3,±0.181(4)).

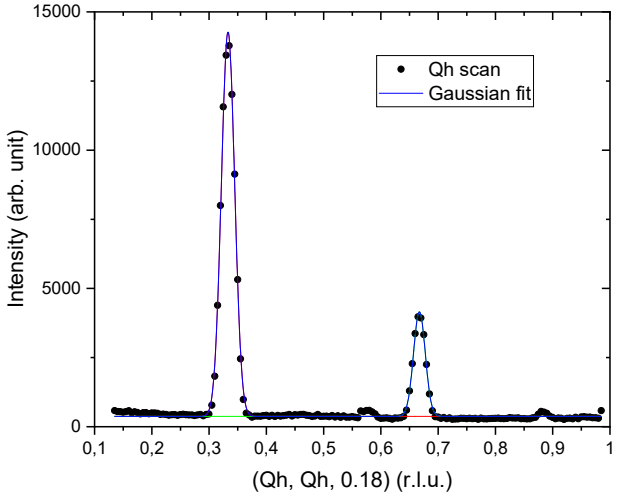

Figure 4.31: One dimensional Qh scan at Ql=0.18 revealing maxim of both magnetic Bragg peaks.

Magnetic Bragg peaks were measured on the new sample as well. Magnetic

Bragg peak was discovered at the same position (see figure 4.32 and 4.33) and were fitted by Gaussian function revealing position Qh = 0.3342(7) with FWHM along Qh 0.0115(7) and Ql = 0.1805(4) with FWHM along Ql 0.0269(4). Results from the new samplehad better quality because we do not observe any parasitic peak in the Ql scan.

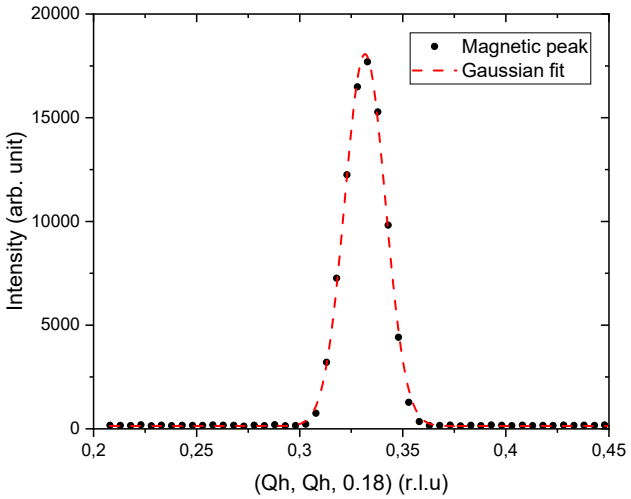

Figure 4.32: Magnetic Bragg peak in new sample, measured along Qh direction

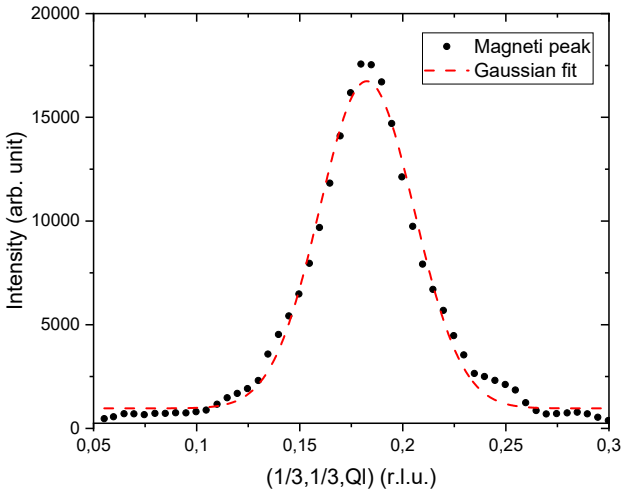

Figure 4.33: Magnetic Bragg peak in new sample, measured along Qh direction

A propagation vector in the ground state was also observed in the D23 experiment. Results from this experiment are consistent with the results above. From the magnetic reflections observed by D23 at temperature 55 mK and in zero magnetic field the magnetic structure of the ground state was determined[2].

[2]Preliminary data refinement of diffraction experiment on D23 done by M. Stekiel.

4.3.3 Spin waves in spin-polarized state

The relatively small critical field of $Na_2BaMn(PO_4)_2$ (around 6 T) allows us to measure spin waves in the spin-polarized state. We measured in the magnetic field of 10 T, where the system is fully polarized. This technique is often used at QSL systems, because it allows determination of coupling constants which could not be accessible in the ground state (47).
The energy dispersion along the (0,0,Ql) direction is shown in figure 4.34 in K (1/3,1/3,Ql) point and in figure 4.35 in M (1/2,1/2,Ql) point. We can see that the dispersion in this direction is flat. The blue line is the linear fit of the centers of Gaussian functions and the error bar is the FWHM of each Gaussian peak fitted for each energy scan. The results of these linear fits are in table 9. The slope of these dispersions is very close to zero suggesting negligible dispersion along the c axis. From the intercepts of linear fit, we can determine the energy gap in these high symmetry points.

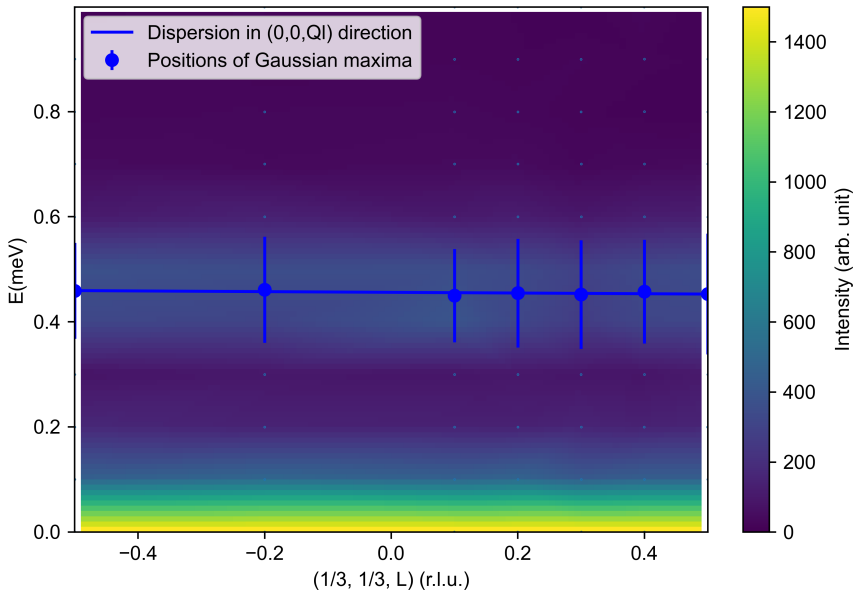

Figure 4.34: Flat spin wave dispersion along (0,0,Ql) at high symmetry point K measured in magnetic field 10 T and temperature 55 mK. Blue dots represent fitted center positions of Gaussian functions and the blue line is the linear fit of this dispersion.

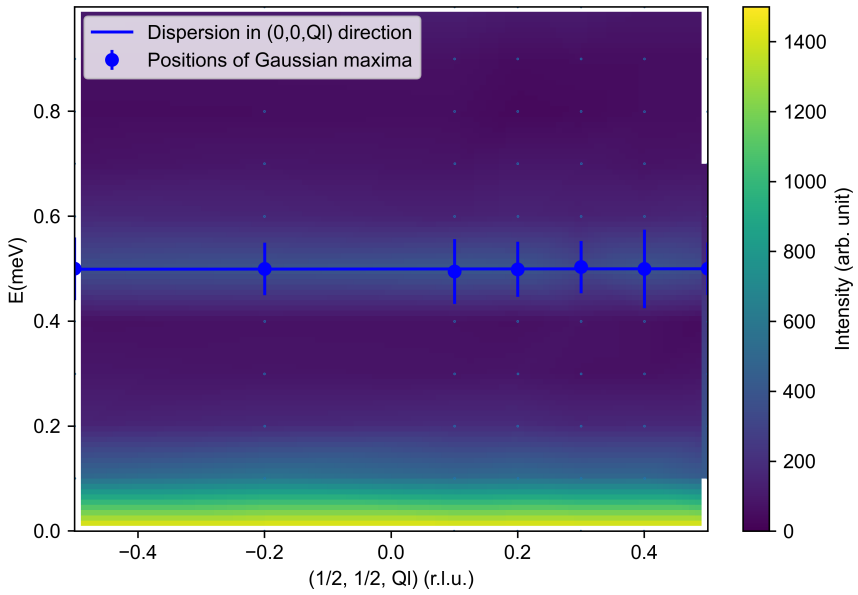

Figure 4.35: Flat spin wave dispersion along (0,0,Ql) at high symmetry point M measured in magnetic field 10 T and temperature 55 mK. Blue dots represent fitted center positions of Gaussian functions and the blue line is the linear fit of this dispersion.

High symmetry point	Slope	Energy gap (meV)
K point	-0.0006(5)	0.455(5)
M point	0.0008(6)	0.499(3)

Table 9: Result of linear fitting of flat dispersion in (0,0,Ql) direction at high symmetry points.

In contrast to the negligible dispersion along c axis, the dispersion in (Qh,Qh,0) plane shows remarkable momentum dependence. This dependence can be described by the model 1.17. We measured the dispersion of the spin waves Qh = 0.2 to Qh = 0.5 and up to energy 1 meV shown in figure 4.36. Obtained parameters from dispersion relation are $J = 0.0299(1)$ meV and $B^* = 0.677(3)$ meV. Additional points were measured, but are not in the figures 4.36 and 4.37, because they do not form map. Additional points are plotted in figure 4.38.
In the dispersion one spin wave excitation is clearly visible, but around Qh = 0.35 another branch appears. This is not a real signal, but an spurios signal coming from (IN12) itself (so called cuppat-axe spurion (24)). To support this statement we present measured dispersion on new sample in figure 4.37. No parasitic branch of spin wave dispersion is observed. We can also see that the background is reduced and the FWHM of the spin wave excitations are smaller.

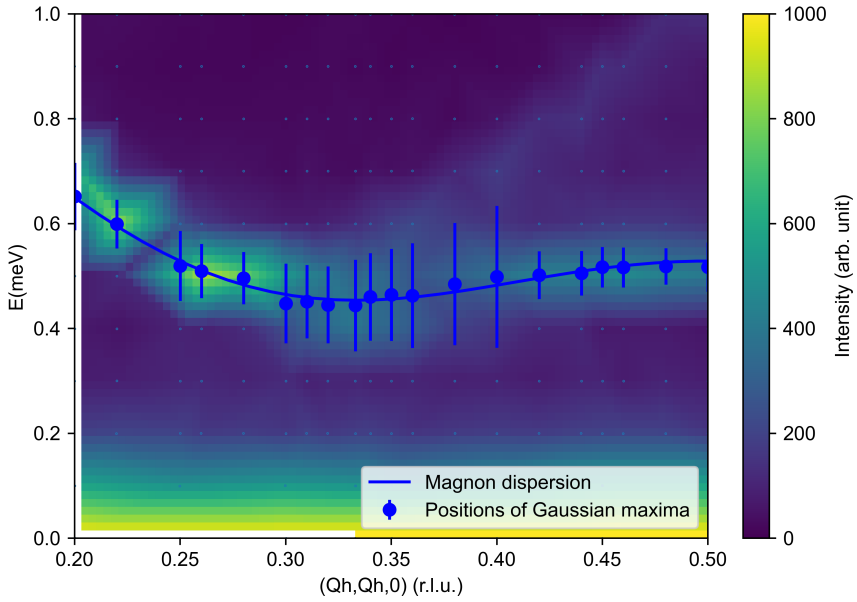

Figure 4.36: Contour maps of the experimental spin-wave dispersion in the fully polarized state, in field B = 10 T and at temperature T = 55 mK. Blue circles with error bars are the fitted center positions, and the solid blue curve is the simulated linear spin wave dispersion.

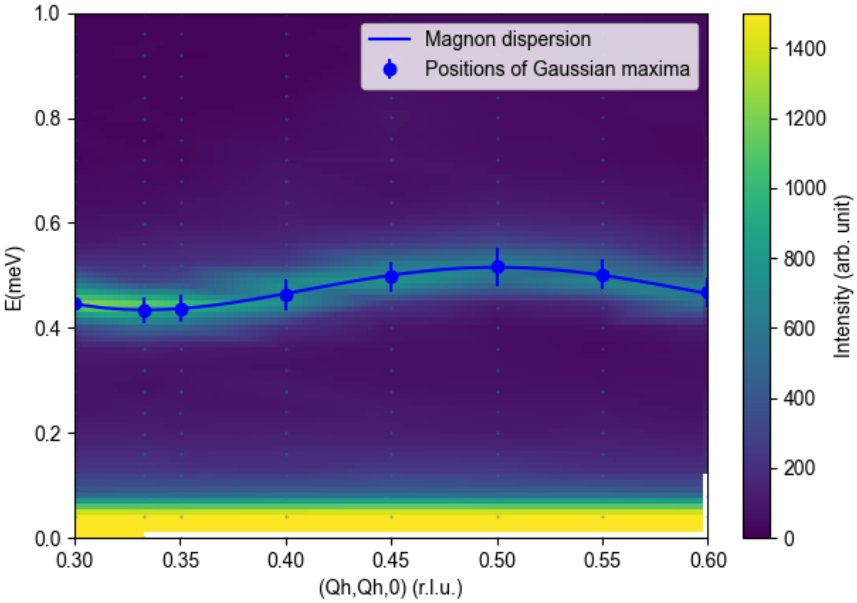

Figure 4.37: Contour maps of the experimental spin-wave dispersion in the fully polarized state in the new sample, in field B = 10 T and at temperature T = 55 mK. Blue circles with error bars are the fitted center positions, and the solid blue curve is the simulated linear spin wave dispersion.

Obtained dispersion of $Na_2BaMn(PO_4)_2$ in fully polarized state was compared

to other measurements on compounds $Na_2BaCo(PO_4)_2$ (28) and $Na_2BaNi(PO_4)_2$ (27) in figure 4.38. The dispersions are scaled for the same magnetic field of 10 T. We can see that a larger magnetic moment leads to a lower spin wave excitations, which is in agreement with the theory that predicts a bigger energy barrier for larger spins.

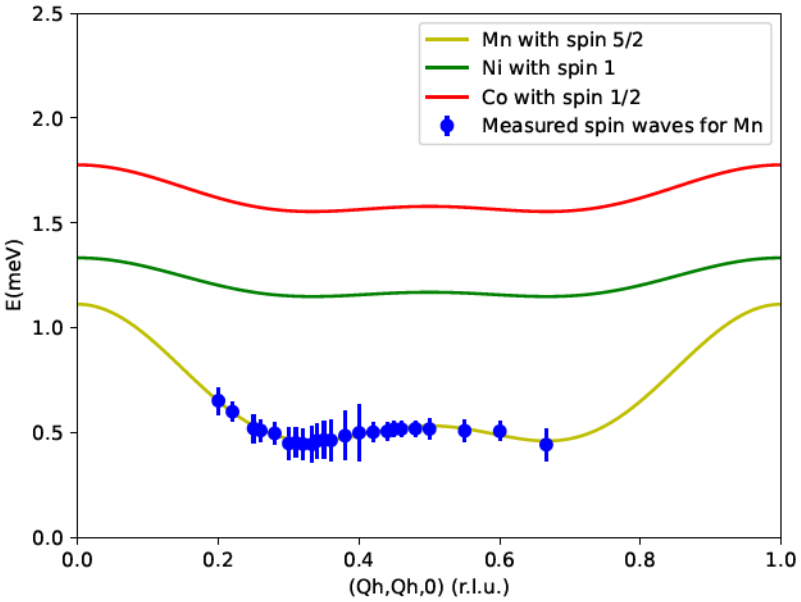

Figure 4.38: Spin waves in the spin-polarized state of $Na_2BaX(PO_4)_2$ (X = Co (28), Ni (27), Mn) all scaled in the magnetic field 10 T and all measured points for $Na_2BaMn(PO_4)_2$.

Measured data were also compared to the simulated data using Monte Carlo calculations through the software Takin in order to take resolution of the instrument into the account. This calculation method is described in Appendix C. Simulated spin waves in the whole range of one Brillouin (from Qh = -0.5 to 0.5) zone are in figure 4.39. The simulations is not scaled to our data. Also to save time our simulation was programmed to return zero, when far from the inelastic signal, which explains the white space above the interesting energy.
We also simulated spectrum to compare to our measured data as shown in figure 4.40.

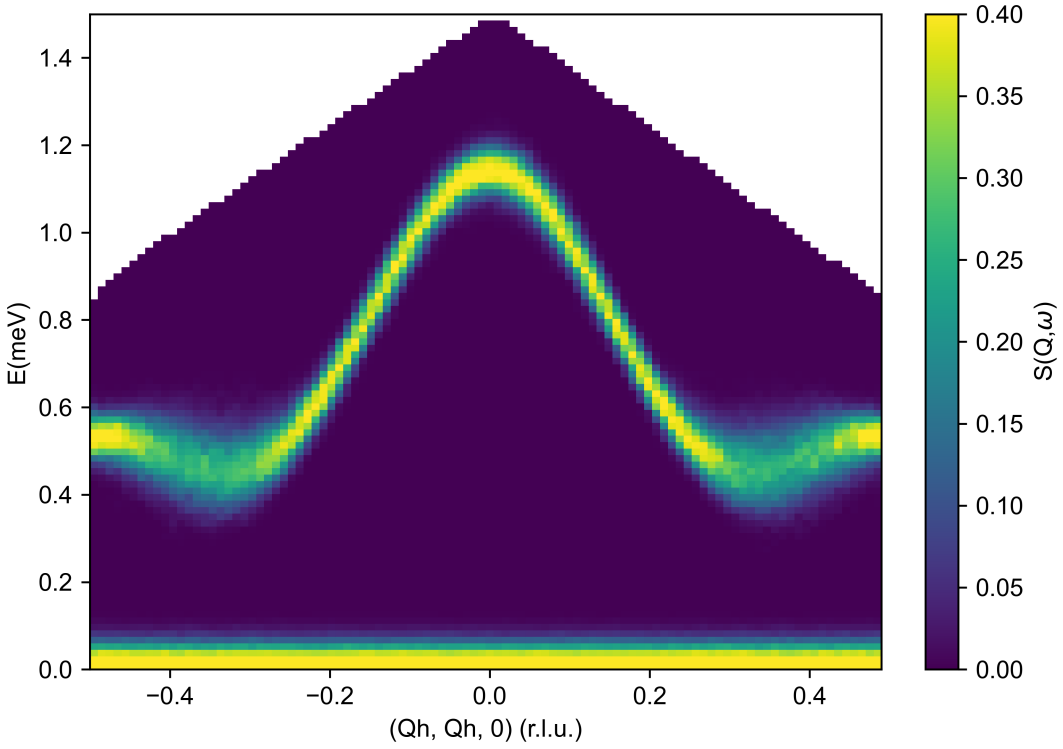

Figure 4.39: Simulated spin wave spectrum using Takin in whole Brillouin zone.

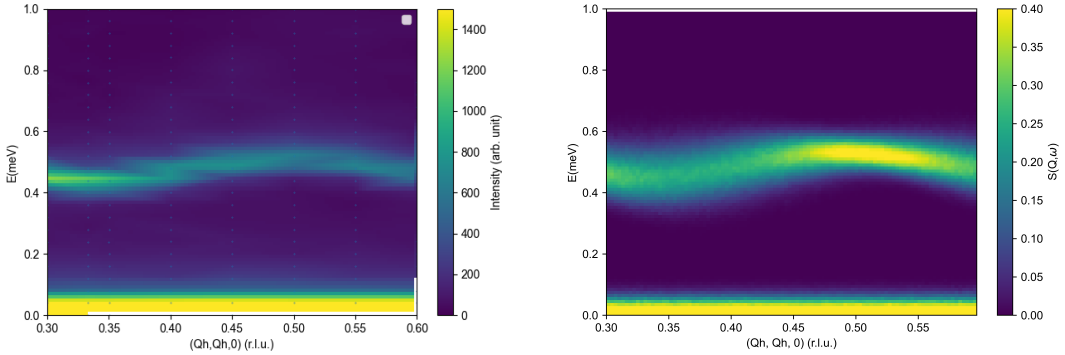

(a) (b)

Figure 4.40: Comparison of a) measured data and b) simulated data by Takin from Qh = 0.3 to 0.6.

5 Conclusions

The goal of this thesis was to a) uncover physics in frustrated magnets b) to develop and test new experimental technique. For this purpose a high- quality single crystals of $Na_2BaMn(PO_4)_2$ were grown using the flux growth method and characterized by Laue diffraction and x-ray powder diffraction, revealing their good quality. The constructed magnetic phase diagram resulting from our heat capacity measurements is in agreement with the previously published one, revealing a complex magnetic phase structure expected for frustrated triangular lattice antiferromagnet. Additionally, we have detected and described previously unreported phase which was initially hidden in the up-up-down phase. This phase was tentatively determined as the Vortex Crystal phase, but further analysis is required and preparatory steps to investigate this exotic quantum phase have already been taken.

As the mass of the crystals of $Na_2BaMn(PO_4)_2$ is typically below 10 mg, it is almost impossible to perform inelastic neutron experiments to study these magnetic phases in detail. Therefore a new experimental device based on robotic arm and robotic vision called ALSA was developed as a part of this thesis. ALSA was used for the preparation of two generations of samples formed by co-aligning hundreds of crystals. The first generation sample prepared by ALSA was analyzed by neutron scattering and several improvements to the preparation technique were made: a new sample holder was developed and crystal placement was improved. The subsequent improvement of ALSA proved to be very successful. We observed significant improvement in data comparing these two generations of samples. ALSA proved to be a reliable help in the laboratory and provided a new and more efficient way to prepare samples. ALSA can co-align samples with mosaic spread under 2°, making it more efficient than human research.

The experiment on co-aligned crystals using ALSA was done in Institute Laue-Langevin using cold neutron triple axis spectrometer. The propagation vector in the ground state of this compound was determined as $\overrightarrow{k} = (1/3, 1/3, \pm 0.181(4))$. In the same experiment, the spin waves in a fully polarized state were observed and they are in good agreement with one magnon dispersion. Our observed data were also compared to isostructural compounds $Na_2BaCo(PO_4)_2$ and $Na_2BaNi(PO_4)_2$. The spin wave dispersion appears to be flat in the Ql direction, revealing a strong Qh dependence on the dispersion spectrum. Magnon dispersion of all three compounds was then compared and it seemed to be mostly dependent on the spin of the magnetic compound as expected.

Both goals a) and b) of this thesis were successfully accomplished.

6 Future Plans

Measurements on the second generation of samples revealed spin waves dispersion in the ground state and other states from the magnetic phase diagram, which were previously hidden in the signal of the elastic line. We are currently in the process of analyzing the data. We are also in the process of refining the data from D23 and determining the magnetic structures of individual phases. Contents of this thesis with measurements of spin waves in other phases and magnetic structure refinement will be published.
We are also improving ALSA and preparing for the distribution of ALSA to the users. ALSA can be used for sample preparation of other promising candidates for inelastic neutron studies who suffer from low masses of available single crystal, such as Henmilite studied by Ankit Labh. We are preparing paper describing algorithms behind ALSA usage.

Appendices

A Dispersion relation of spin waves

Compounds $Na_2BaM(PO_4)_2$ (M = Co, Ni, Mn) are two-dimensional triangular lattice antiferromagnetic systems so we can rewrite Hamiltonian in equation 1.6 into the XXZ-Hamiltonian

$$H = \sum_{\langle ij \rangle} \left[J \left(S_i^x S_j^x + S_i^y S_j^y \right) + \Delta S_i^z S_j^z \right] + g\mu_B \sum_i \mathbf{B} \cdot \mathbf{S} \tag{A.1}$$

For simplicity of calculations, we will focus on the first term in Hamiltonian without a magnetic field. Now we rewrite the whole Hamiltonian in the non-Hermitian ladder operators defined by

$$S_i^x = \frac{1}{2} \left(S_i^+ + S_i^- \right) \tag{A.2}$$

$$S_i^y = \frac{1}{2i} \left(S_i^+ - S_i^- \right) \tag{A.3}$$

To obtain the S_i^z component we use the normalisation of spin $(S^x)^2 + (S^y)^2 + (S^z)^2 = 1$ and expand the square root $\sqrt{1-x} \approx 1 - \frac{x}{2}$. After substituting it into equation A.1 we obtain

$$H = \sum_{\langle ij \rangle} \left[J \left(S_i^+ S_j^- + S_i^- S_j^+ \right) + \Delta \left(1 + \frac{(S_i^x)^2}{2} + \frac{(S_i^y)^2}{2} - \frac{(S_j^x)^2}{2} - \frac{(S_j^y)^2}{2} \right) \right] \tag{A.4}$$

Now to solve equation A.4 we apply linear spin wave theory. The spin operators are expanded in terms of creation and annihilation operators on every magnetic site in the local coordinate system. By keeping only the lowest order of the operator we create a linear approximation of the complex spin dynamics (48):

$$S_i^+ = \sqrt{2S} a_i^\dagger \tag{A.5}$$

$$S_i^- = \sqrt{2S} a_i \tag{A.6}$$

$$\tag{A.7}$$

and we obtain Hamiltonian in terms of creation and annihilation operators.

$$H = \sum_{\langle ij \rangle} \left[SJ \left(a_i^\dagger a_j + a_i a_j^\dagger \right) + \Delta \left(1 + 4S \left(a_i^\dagger a_i - a_j^\dagger a_j \right) \right) \right] \tag{A.8}$$

Now we apply the Fourier transform of creation and annihilation operators (49)

$$a_i^{(\dagger)} = \frac{1}{\sqrt{N}} \sum_k a_k^{(\dagger)} e^{(\pm i \mathbf{k} \cdot \mathbf{r}_i)} \tag{A.9}$$

where $\mathbf{k} = (k_x, k_y)$ is the propagation vector, which we assume to be two-dimensional and we substitute that in

$$H = \sum_{\langle ij \rangle} \left[\frac{SJ}{N} \sum_k a_k^\dagger a_k \left(2\cos(\mathbf{k}(\mathbf{r}_j - \mathbf{r}_i)) \right) + \Delta \right] \tag{A.10}$$

Now we need to exchange sums and sum over nearest neighbors in a triangular lattice. There are six nearest neighbors in a triangular lattice, but we just need to sum over three neighbors with vectors

$$\begin{aligned} r_1 &= (1, 0) \\ r_2 &= (1/2, \sqrt{3}/2) \\ r_3 &= (-1/2, \sqrt{3}/2) \end{aligned}$$

and multiply the whole term by 2 because cosine is an even function. The Hamiltonian simplifies

$$H = 2\frac{SJ}{N}\sum_k a_k^\dagger a_k \left(\cos k_x + 2\cos\frac{k_x}{2}\cos\frac{\sqrt{3}k_y}{2}\right) + \Delta \tag{A.11}$$

Now we just need to diagonalize this Hamiltonian, which is straightforward (50) obtaining the equation

$$E(k) = 2SJ\left[\cos k_x + 2\cos\frac{k_x}{2}\cos\frac{\sqrt{3}k_y}{2}\right] + B^* \tag{A.12}$$

where in B^* we combined the Δ and Zeeman term from the beginning.

B IN12

IN12 is a triple-axis spectrometer using cold neutrons. That means that neutrons guided to the instrument by neutron guide are moderated by so called cold sorces at temperature 4 K. The layout of IN12 is in figure B.1. The initial white neutron beam comes from neutron guide H144 and the velocity selector selects a wavelength band that continues through the neutron guide to the monochromator. The monochromator is a single crystal of pyrolytic graphite (002) which selects an initial wavelength using Bragg's law and directs a neutron beam onto the sample. Then the beam interacts with the sample and is scattered in many different directions and with different energies. This change in direction and energy is what we want to detect. To measure the energy of the scattered beam the secondary spectrometer, comprising the analyzer and detector, is used. The secondary spectrometer is moved to choose the direction of measuring the final intensity, and the analyzer and detector are then set to measure neutrons at the final wavelength. The intensity of the scattered neutron bean is measured while scanning the initial or final wavelengths.

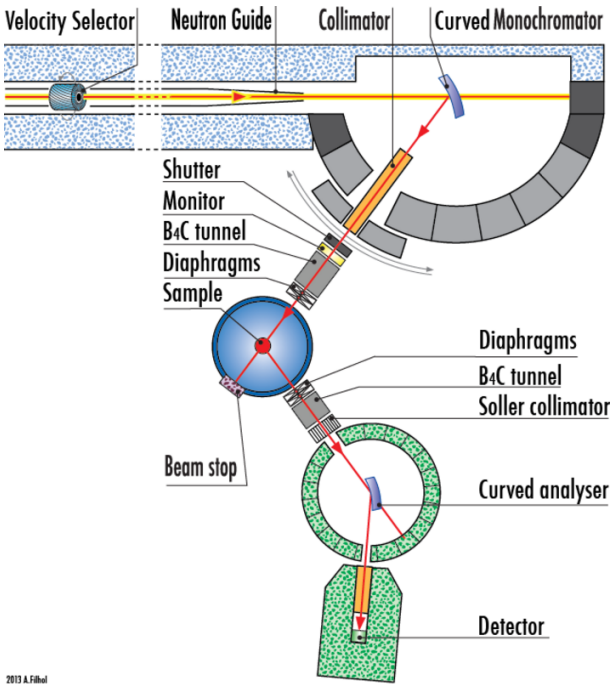

Figure B.1: The layout of cold neutron triple axis spectrometer (51).

C Introduction to Takin data analysis

Software suite Takin (52) is used to perform convolution of a physical system's dynamical structure factor S(**Q**, E) and the instrument resolution function (53). S(**Q**, ω) function is provided via Python script.
Triple-axis spectrometers are very versatile instruments for inelastic neutron scattering. All magnetic and nuclear excitations can be investigated by measuring intensity in arbitrary points in four-dimensional momentum (Q) and energy (ω) space. This means that we need to know the four-dimensional resolution function of our instrument. Because the doubly-curved monochromators are used, we need to use the resolution dependent on the actual position in real space where the scattering event takes place (shown in figure C.1).

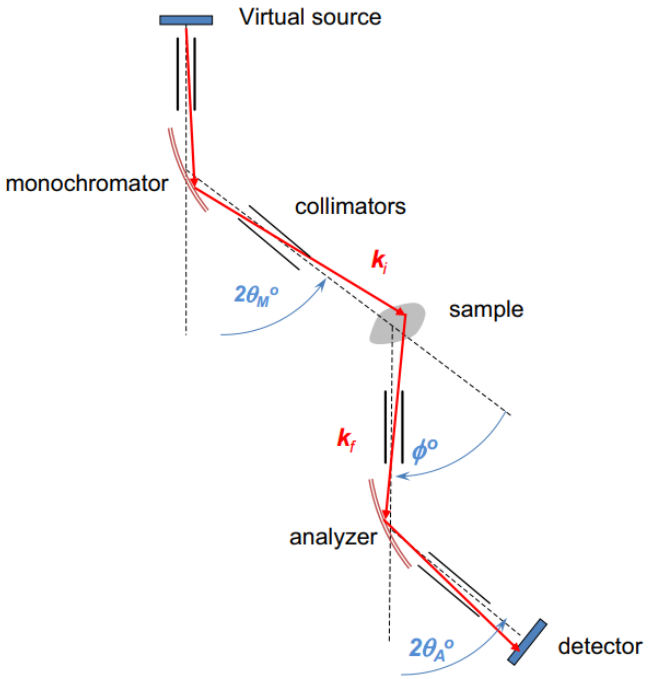

Figure C.1: Layout of a three-axis spectrometer along with different beam paths that have to be considered in resolution calculations. The dashed lines represent the optical axes and correspond to the nominal setting of the spectrometer characterized by wave vectors k_i^0 and k_f^0 for the incident and scattered neutrons, respectively (54).

The scattered neutron intensity is represented by

$$I(\mathbf{k}_i^0, \mathbf{k}_f^0) = \int_V d\mathbf{r} \int d\mathbf{k}_i W_i(\mathbf{r}, \mathbf{k}_i) \int d\mathbf{k}_i W_f(\mathbf{r}, \mathbf{k}_f) S(\mathbf{Q}, \omega) \tag{C.1}$$

$W_i(\mathbf{r}, \mathbf{k}_i)$ is the probability that a neutron with a particular wave vector $\mathbf{k}_i$ hits the sample at $\mathbf{r}$, and $W_f(\mathbf{r}, \mathbf{k}_f)$ is the probability that a neutron with some wave vector $\mathbf{k}_f$ that is scattered at $\mathbf{r}$ is actually registered in the detector. In Gaussian approximation, the resolution function can be characterized by the so-called resolution ellipsoid that is the surface in ($\mathbf{Q}$,ω)-space (54). The orientation of this ellipsoid is determined by the coupling of momentum and energy resolution.

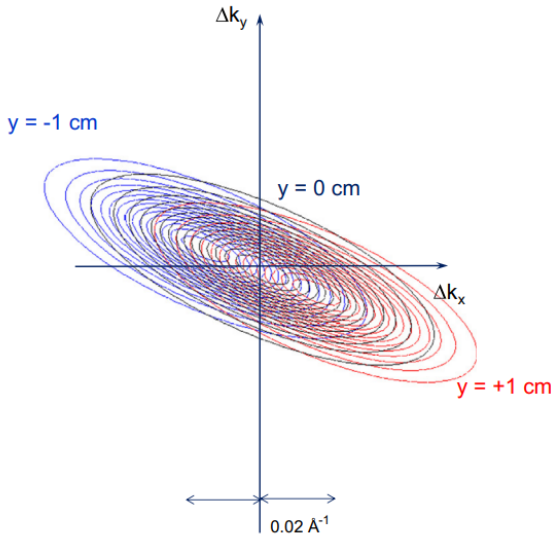

Figure C.2: Resolution ellipsoid for $k_i = 2.662\mathring{A}$ using a monochromator at the center of the optical path (black) and $\pm$ 1 cm displaced (blue and red) using flat monochromator with open collimators (54).

For a flat monochromator the ellipsoid is rotated and its orientation becomes almost parallel to the monochromator crystal (see figure C.2) since higher energy neutrons (corresponding to larger k_x) are predominantly reflected under smaller angles. Again, there is a shift of the center with y. However due to the large extension of the ellipsoid along Δk_x, this effect is hidden by the smearing of the resolution.

Bibliography

[1] M. F. Collins and O. A. Petrenko, "Review/synthèse: Triangular antiferromagnets," *Canadian Journal of Physics*, vol. 75, no. 9, pp. 605–655, 1997. [Online]. Available: https://doi.org/10.1139/p97-007

[2] A. V. Chubukov and D. I. Golosov, "Quantum theory of an antiferromagnet on a triangular lattice in a magnetic field," *Journal of Physics: Condensed Matter*, vol. 3, no. 1, p. 69, jan 1991. [Online]. Available: https://dx.doi.org/10.1088/0953-8984/3/1/005

[3] J. Alicea, A. V. Chubukov, and O. A. Starykh, "Quantum stabilization of the 1/3-magnetization plateau in cs_2cubr_4," *Phys. Rev. Lett.*, vol. 102, p. 137201, Mar 2009. [Online]. Available: https://link.aps.org/doi/10.1103/PhysRevLett.102.137201

[4] M. Swanson, J. T. Haraldsen, and R. S. Fishman, "Publisher's note: Critical anisotropies of a geometrically frustrated triangular-lattice antiferromagnet [phys. rev. b 79, 184413 (2009)]," *Phys. Rev. B*, vol. 79, p. 189902, May 2009. [Online]. Available: https://link.aps.org/doi/10.1103/PhysRevB.79.189902

[5] D. Yamamoto, G. Marmorini, and I. Danshita, "Microscopic model calculations for the magnetization process of layered triangular-lattice quantum antiferromagnets," *Phys. Rev. Lett.*, vol. 114, p. 027201, Jan 2015. [Online]. Available: https://link.aps.org/doi/10.1103/PhysRevLett.114.027201

[6] N. Li, Q. Huang, X. Y. Yue, W. J. Chu, Q. Chen, E. S. Choi, X. Zhao, H. D. Zhou, and X. F. Sun, "Possible itinerant excitations and quantum spin state transitions in the effective spin-1/2 triangular-lattice antiferromagnet na2baco(po4)2," *Nature Communications*, vol. 11, no. 1, p. 4216, Aug 2020. [Online]. Available: https://doi.org/10.1038/s41467-020-18041-3

[7] N. Li, Q. Huang, A. Brassington, X. Y. Yue, W. J. Chu, S. K. Guang, X. H. Zhou, P. Gao, E. X. Feng, H. B. Cao, E. S. Choi, Y. Sun, Q. J. Li, X. Zhao, H. D. Zhou, and X. F. Sun, "Quantum spin state transitions in the spin-1 equilateral triangular lattice antiferromagnet $na_2BaNi(PO_4)_2$," *Phys. Rev. B*, vol. 104, p. 104403, Sep 2021. [Online]. Available: https://link.aps.org/doi/10.1103/PhysRevB.104.104403

[8] J. Kim, K. Kim, E. Choi, Y. J. Ko, D. W. Lee, S. H. Lim, J. H. Jung, and S. Lee, "Magnetic phase diagram of a 2-dimensional triangular lattice antiferromagnet na2bamn(po4)2," *Journal of Physics: Condensed*

Matter, vol. 34, no. 47, p. 475803, oct 2022. [Online]. Available: https://dx.doi.org/10.1088/1361-648X/ac965f

[9] C. Liu, P. Bourges, Y. Sidis, T. Xie, G. He, F. Bourdarot, S. Danilkin, H. Ghosh, S. Ghosh, X. Ma, S. Li, Y. Li, and H. Luo, "Preferred spin excitations in the bilayer iron-based superconductor $CaK(Fe_{0.96}Ni_{0.04})_4as_4$ with spin-vortex crystal order," *Phys. Rev. Lett.*, vol. 128, p. 137003, Mar 2022. [Online]. Available: https://link.aps.org/doi/10.1103/PhysRevLett.128.137003

[10] S. Blundell, *Magnetism in Condensed Matter*. Oxford University Press, 2001.

[11] K. H. J. Buschow, *Physics of Magnetism and Magnetic Materials*. Springer New York, 2012.

[12] R. White, *Quantum Theory of Magnetism*, ser. Springer series in solid-state sciences. Springer-Verlag, 1983. [Online]. Available: https://books.google.cz/books?id=fUssAAAAYAAJ

[13] M. Vališka, "Interplay between crystal structure and magnetism of the rare earth intermetallics," 2011.

[14] D. Givord, *Introduction to Magnetism and Magnetic Materials*. Berlin, Heidelberg: Springer Berlin Heidelberg, 2001. [Online]. Available: https://doi.org/10.1007/3-540-44954-X_1

[15] H. A. Mugiraneza, S., "Tutorial: a beginner's guide to interpreting magnetic susceptibility data with the Curie-Weiss law." *Communications Physics*, vol. 5, no. 95, 2022.

[16] M. S. Dresselhaus, *Magnetic Properties of Solids*. New York University, 2001.

[17] M. Vojta, "Frustration and quantum criticality," p. 064501, may 2018. [Online]. Available: https://dx.doi.org/10.1088/1361-6633/aab6be

[18] O. A. Starykh, "Unusual ordered phases of highly frustrated magnets: a review," *Reports on Progress in Physics*, vol. 78, no. 5, p. 052502, apr 2015. [Online]. Available: https://dx.doi.org/10.1088/0034-4885/78/5/052502

[19] L. Balents, "Spin liquids in frustrated magnets," *Nature*, vol. 464, no. 7286, pp. 199–208, Mar 2010. [Online]. Available: https://doi.org/10.1038/nature08917

[20] Y. Zhou, K. Kanoda, and T.-K. Ng, "Quantum spin liquid states," *Rev. Mod. Phys.*, vol. 89, p. 025003, Apr 2017. [Online]. Available: https://link.aps.org/doi/10.1103/RevModPhys.89.025003

[21] L. Savary and L. Balents, "Quantum spin liquids: a review," *Reports on Progress in Physics*, vol. 80, no. 1, p. 016502, nov 2016. [Online]. Available: https://dx.doi.org/10.1088/0034-4885/80/1/016502

[22] J. R. Chamorro, T. M. McQueen, and T. T. Tran, "Chemistry of quantum spin liquids," *Chemical Reviews*, vol. 121, no. 5, pp. 2898–2934, Mar 2021. [Online]. Available: https://doi.org/10.1021/acs.chemrev.0c00641

[23] C. Kittel, *Introduction to Solid State Physics*. Wiley, 2004.

[24] A. Boothroyd, *Principles of Neutron Scattering from Condensed Matter*. Oxford University Press, 2020. [Online]. Available: https://books.google.cz/books?id=y2JuzQEACAAJ

[25] R. Zhong, S. Guo, G. Xu, Z. Xu, and R. J. Cava, "Strong quantum fluctuations in a quantum spin liquid candidate with a co-based triangular lattice," *Proceedings of the National Academy of Sciences*, vol. 116, no. 29, pp. 14 505–14 510, 2019. [Online]. Available: https://www.pnas.org/doi/abs/10.1073/pnas.1906483116

[26] F. Ding, Y. Ma, X. Gong, D. Hu, J. Zhao, L. Li, H. Zheng, Y. Zhang, Y. Yu, L. Zhang, F. Zhao, and B. Pan, "Structure and frustrated magnetism of the two-dimensional triangular lattice antiferromagnet na2bani(po4)2*," *Chinese Physics B*, vol. 30, no. 11, p. 117505, nov 2021. [Online]. Available: https://dx.doi.org/10.1088/1674-1056/abff1d

[27] J. Sheng, J.-W. Mei, L. Wang, W. Jiang, L. Xu, H. Ge, N. Zhao, T. Li, A. Candini, B. Xi, J. Zhao, Y. Fu, J. Yang, Y. Zhang, G. Biasiol, S. Wang, J. Zhu, P. Miao, X. Tong, D. Yu, R. Mole, L. Ma, Z. Zhang, Z. Ouyang, W. Tong, A. Podlesnyak, L. Wang, F. Ye, D. Yu, L. Wu, and Z. Wang, "Bose-einstein condensation of a two-magnon bound state in a spin-one triangular lattice," 2023.

[28] J. Sheng, L. Wang, A. Candini, W. Jiang, L. Huang, B. Xi, J. Zhao, H. Ge, N. Zhao, Y. Fu, J. Ren, J. Yang, P. Miao, X. Tong, D. Yu, S. Wang, Q. Liu, M. Kofu, R. Mole, G. Biasiol, D. Yu, I. A. Zaliznyak, J.-W. Mei, and L. Wu, "Two-dimensional quantum universality in the spin-1/2 triangular-lattice quantum antiferromagnet na¡sub¿2¡/sub¿baco(po¡sub¿4¡/sub¿)¡sub¿2¡/sub¿," *Proceedings of the National Academy of Sciences*, vol. 119, no. 51, p. e2211193119, 2022. [Online]. Available: https://www.pnas.org/doi/abs/10.1073/pnas.2211193119

[29] D. Nishio-Hamane, T. Minakawa, and H. Okada, "Iwateite, na2bamn (po4) 2, a new mineral from the tanohata mine, iwate prefecture, japan," *Journal of Mineralogical and Petrological Sciences*, vol. 109, no. 1, pp. 34–37, 2014.

[30] G. Nakayama, S. Hara, H. Sato, Y. Narumi, and H. Nojiri, "Synthesis and magnetic properties of a new series of triangular-lattice magnets, na2bamv2o8 (m = ni, co, and mn)," *Journal of Physics: Condensed Matter*, vol. 25, no. 11, p. 116003, feb 2013. [Online]. Available: https://dx.doi.org/10.1088/0953-8984/25/11/116003

[31] L. D. Sanjeewa, V. O. Garlea, M. A. McGuire, C. D. McMillen, and J. W. Kolis, "Magnetic ground state crossover in a series of glaserite systems with triangular magnetic lattices," *Inorganic*

Chemistry, vol. 58, no. 4, pp. 2813–2821, 2019. [Online]. Available: https://doi.org/10.1021/acs.inorgchem.8b03418

[32] C. Liu, P. Bourges, Y. Sidis, T. Xie, G. He, F. Bourdarot, S. Danilkin, H. Ghosh, S. Ghosh, X. Ma, S. Li, Y. Li, and H. Luo, "Preferred spin excitations in the bilayer iron-based superconductor $CaK(Fe_{0.96}Ni_{0.04})_4as_4$ with spin-vortex crystal order," *Phys. Rev. Lett.*, vol. 128, p. 137003, Mar 2022. [Online]. Available: https://link.aps.org/doi/10.1103/PhysRevLett.128.137003

[33] C. Koughia, S. Kasap, and P. Capper, *Springer Handbook of Electronic and Photonic Materials*. Berlin, Heidelberg: Springer-Verlag, 2007.

[34] I. Pritula and K. Sangwal, "29 - fundamentals of crystal growth from solutions," in *Handbook of Crystal Growth (Second Edition)*, second edition ed., ser. Handbook of Crystal Growth, P. Rudolph, Ed. Boston: Elsevier, 2015, pp. 1185–1227. [Online]. Available: https://www.sciencedirect.com/science/article/pii/B9780444633033000298

[35] Y. Shiohara and T. Izumi, "30 - crystallization mechanisms of high critical temperature superconductors," in *Handbook of Crystal Growth (Second Edition)*, second edition ed., ser. Handbook of Crystal Growth, P. Rudolph, Ed. Boston: Elsevier, 2015, pp. 1229–1275. [Online]. Available: https://www.sciencedirect.com/science/article/pii/B9780444633033000304

[36] S. Dagdale, V. Pahurkar, and G. Muley, "High temperature crystal growth: An overview," *Macromolecular Symposia*, vol. 362, no. 1, pp. 139–141, 2016. [Online]. Available: https://onlinelibrary.wiley.com/doi/abs/10.1002/masy.201400254

[37] "Detection of ArUco markers," https://docs.opencv.org/4.x/d5/dae/tutorial_aruco_detection.html#:~:text=An%20ArUco%20marker%20is%20a,determines%20its%20identifier%20(id)., Accessed: 2024-01-30.

[38] D. Wałoszek, "Real application of online 2d irregullar bin packing," 2021.

[39] K. C. Rule, R. A. Mole, and D. Yu, "Which glue to choose? a neutron scattering study of various adhesive materials and their effect on background scattering," *Journal of Applied Crystallography*, vol. 51, no. 6, pp. 1766–1772, 2018.

[40] "Python library OpenCV," https://opencv.org/, Accesed: 2024-02-20.

[41] R. Ishii, S. Tanaka, K. Onuma, Y. Nambu, M. Tokunaga, T. Sakakibara, N. Kawashima, Y. Maeno, C. Broholm, D. P. Gautreaux, J. Y. Chan, and S. Nakatsuji, "Successive phase transitions and phase diagrams for the quasi-two-dimensional easy-axis triangular antiferromagnet rb4mn(moo4)3," *Europhysics Letters*, vol. 94, no. 1, p. 17001, mar 2011. [Online]. Available: https://dx.doi.org/10.1209/0295-5075/94/17001

[42] L. E. Svistov, A. I. Smirnov, L. A. Prozorova, O. A. Petrenko, L. N. Demianets, and A. Y. Shapiro, "Quasi-two-dimensional antiferromagnet on a triangular lattice RbFe$(moo_4)_2$," *Phys. Rev. B*, vol. 67, p. 094434, Mar 2003. [Online]. Available: https://link.aps.org/doi/10.1103/PhysRevB.67.094434

[43] L. Seabra, P. Sindzingre, T. Momoi, and N. Shannon, "Novel phases in a square-lattice frustrated ferromagnet : $\frac{1}{3}$-magnetization plateau, helicoidal spin liquid, and vortex crystal," *Phys. Rev. B*, vol. 93, p. 085132, Feb 2016. [Online]. Available: https://link.aps.org/doi/10.1103/PhysRevB.93.085132

[44] N. Biniskos, P. Cermak, K. Schmalzl, P. Steffens, D. Svitak, and M.Valiska, "Measured as part of proposal: "Investigating the spin excitations in the two dimensional antiferromagnet Na2BaMn(PO4)2"," 2023.

[45] J. K. J. S. R. K. S. D. S. A. Labh, N. Biniskos, "Measured as part of proposal: "spin excitations of Na2BaMn(PO4)2 in the disordered state"," 2024.

[46] "Instrument orientexpress," https://www.ill.eu/users/instruments/instruments-list/orientexpress/description/instrument-layout, Accessed: 2024-04-12.

[47] A. K. Bera, J. Wu, W. Yang, R. Bewley, M. Boehm, J. Xu, M. Bartkowiak, O. Prokhnenko, B. Klemke, A. N. Islam *et al.*, "Dispersions of many-body bethe strings," *Nature Physics*, vol. 16, no. 6, pp. 625–630, 2020.

[48] S. Toth and B. Lake, "Linear spin wave theory for single-q incommensurate magnetic structures," *Journal of Physics: Condensed Matter*, vol. 27, no. 16, p. 166002, mar 2015. [Online]. Available: https://dx.doi.org/10.1088/0953-8984/27/16/166002

[49] D. D. S. Anil Prabhakar, *Spin Waves, Theory and Applications*. Springer New York, NY, 2009.

[50] F. Schwabl, *Advanced Quantum Mechanics*. Springer Berlin, Heidelberg, 2008.

[51] "Instrument cold neutron triple axis spectrometer," https://www.ill.eu/users/instruments/instruments-list/d23/description/instrument-layout, Accessed: 2024-04-12.

[52] T. Weber, "Takin 2," Feb. 2024. [Online]. Available: https://doi.org/10.5281/zenodo.10656089

[53] ——, "Update 2.5 to "takin: An open-source software for experiment planning, visualisation, and data analysis",(pii: S2352711016300152)," *SoftwareX*, vol. 23, p. 101471, 2023.

[54] G. Eckold and O. Sobolev, "Analytical approach to the 4d-resolution function of three axes neutron spectrometers with focussing monochromators and analysers," *Nuclear Instruments and Methods in Physics Research Section A: Accelerators, Spectrometers, Detectors and Associated Equipment*, vol. 752, pp. 54–64, 2014. [Online]. Available: https://www.sciencedirect.com/science/article/pii/S0168900214002940